Digitally Twinned Additive Manufacturing: Detecting Flaws in Laser Powder Bed Fusion by Combining Thermal Simulations with In-situ Meltpool Sensor Data.

R. Yavari[1], A. Riensche[1], E. Tekerek[2], L. Jacquemetton[3], H. Halliday[4], M. Vandever[4], A. Tenequer[4],V. Perumal[2], A. Kontsos[2], Z. Smoqi[1], K. Cole[1], P. Rao[1]

[1]Mechanical and Materials Engineering, University of Nebraska-Lincoln, Lincoln, NE.
[2]Mechanical Engineering and Mechanics, Drexel University, Philadelphia, PA.
[3]SigmaLabs, Santa Fe, NM.
[4]Navajo Technical University, Crownpoint, NM.

The goal of this research is the in-situ detection of flaw formation in metal parts made using the laser powder bed fusion (LPBF) additive manufacturing process. This is an important area of research, because, despite the considerable cost and time savings achieved, precision-driven industries, such as aerospace and biomedical, are reticent in using LPBF to make safety-critical parts due to tendency of the process to create flaws. Another emerging concern in LPBF, and additive manufacturing in general, is related to cyber security – malicious actors may tamper with the process or plant flaws inside a part to compromise its performance. Accordingly, the objective of this work is to develop and apply a physics and data integrated strategy for online monitoring and detection of flaw formation in LPBF parts. The approach used to realize this objective is based on combining (twinning) in-situ meltpool temperature measurements with a graph theory-based thermal simulation model that rapidly predicts the temperature distribution in the part (thermal history). The novelty of the approach is that the temperature distribution predictions provided by the computational thermal model were updated layer-by-layer with in-situ meltpool temperature measurements. This *digital twin* approach is applied to detect flaw formation in stainless steel (316L) impeller-shaped parts made using a commercial LPBF system. Four such impellers are produced emulating three pathways of flaw formation in LPBF parts, these are: changes in the processing parameters (process drifts); machine-related malfunctions (lens delamination), and deliberate tampering with the process to plant flaws inside the part (cyber intrusions). The severity and nature of the resulting flaws, such as porosity and microstructure heterogeneity, are characterized ex-situ using X-ray computed tomography, optical and scanning electron microscopy, and electron backscatter diffraction. The digital twin approach is shown to be effective for detection of the three types of flaw formation causes studied in this work.

Keywords: Laser powder bed fusion, Digital Twin, Meltpool monitoring, Flaw detection, Thermal Simulations.

1 Introduction

1.1 Motivation

In laser powder bed fusion (LPBF, Figure 1) layers of metal powder are deposited and selectively melted using thermal energy from a laser [1]. The LPBF process can create complex geometries that are difficult, if not impossible, to manufacture using conventional subtractive or formative processes [2]. Despite its ability to transcend design and manufacturing barriers, as well as reduce cost and lead times, the use of LPBF in safety-critical industries is currently limited due to its tendency to create flaws [3, 4]. Common LPBF flaws include non-uniform (heterogeneous) microstructure within a part, lack-of-fusion and gas porosity, distortion and cracking of part due to residual stresses, poor surface finish, recoater crashes, and failure of anchoring supports [5-8]. Hence, an important research area in LPBF is the online monitoring, detection, and prevention of flaw formation in the part as it is being printed, ultimately culminating in the rapid and reliable in-process qualification of part quality [2, 9-13].

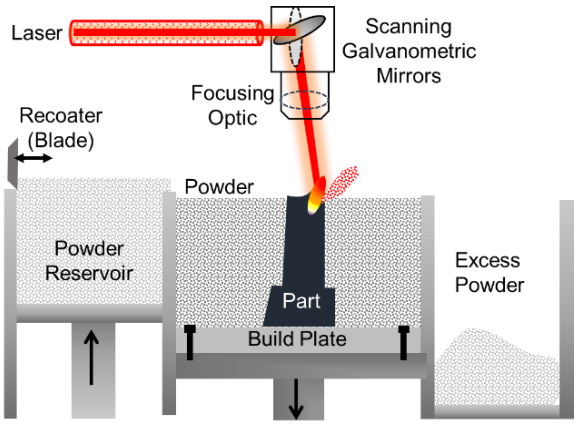

Figure 1: A schematic of the laser powder bed fusion (LPBF) process. Layers of powder are raked on a build plate and selectively melted by a rapidly scanning laser.

Flaw formation in LPBF is generally linked to the complex thermal phenomena involved in melting, cooling, solidification and remelting of powder by the laser [1, 14, 15]. To explain further, the thermal aspects of LPBF that govern flaw formation can be categorized at two broad levels [14-17]. First, at the micro-scale, the melting of the powder material creates a wake of molten

material, called the meltpool, in the order of approximately 100 μm in size (depending on the material characteristics and process parameters) [16]. The temperature distribution, shape (flow), and ejecta (spatter characteristics) of the meltpool are known to influence the resulting microstructure, porosity, and cracking at the granular level [3, 18].

Second, at the macro-scale or part-level, which is in the order of millimeters, the rapid scanning action of the laser and the continuous melting of material at high temperature causes heating and cooling cycles with rates nearing 10^6 °C·s^{-1} and 10^5 °C·s^{-1}, respectively [19-21]. The steep temperature gradients coupled with non-uniform spatiotemporal temperature distributions at the part-level, called the thermal history, are linked to residual stresses, part deformation, and potential material phase transformations [22-25].

The meltpool and part-level thermal interactions leading to flaw formation in as-built LPBF parts are influenced by the following six factors [5, 7, 10, 19, 26-32]: (1) processing parameters, such as laser power, velocity, hatch spacing, scanning pattern; (2) part design, including part shape, orientation and nature of support structures; (3) number, shape and location of other parts on the build plate (build layout); (4) properties of the feedstock powder material, including distribution of powder particles, thermal conductivity, gas entrapment, and contaminants, among others; (5) process faults (drifts or deviations) caused by machine-related anomalies; and (6) malicious cyber intrusions aimed at altering the printing process or part design.

The objective of this work is to develop and apply a physics and data integrated strategy to monitor and detect flaw formation in LPBF parts. The approach used to achieve this objective combines temperature measurements at the meltpool-level provided by appropriate in-situ sensor data with fast and accurate part-level thermal simulations. Such a *digital twin* that integrates physics-based simulations and in-situ sensor data has the potential to provide opportune feedback

for correcting incipient anomalies, thereby reducing waste from failed parts [33-36]. The rationale and need for such a physics-based strategy to detect flaw formation in LPBF is motivated in the context of the drawbacks of using a purely data-driven approach in the forthcoming section.

1.2 Challenges in Data-Driven Flaw Monitoring in LPBF

There is substantial ongoing research to detect flaw formation in LPBF parts by analyzing signatures acquired from in-situ sensor arrays designed to capture meltpool- and part-level phenomena [11, 27, 37-39]. Sensing approaches to track the meltpool behavior used in prior research involve high-speed imaging, thermal imaging, and optical spectroscopy. Popular part-scale flaw monitoring approaches include tracking the layer temperature with infrared thermal cameras, and imaging the powder bed with an optical camera, among others [3, 9, 13, 40-42].

There are three drawbacks in applying a purely sensor data-driven approach for flaw monitoring of LPBF that motivate the need for a physics and data integrated strategy, these are: (i) latency of detection (ii) poor generalizability of data-driven models to different part shapes and layouts; and (iii) resource-intensive nature of acquiring data [9, 36, 37, 43]. These are explained herewith.

(1) Latency in acquiring and analyzing sensor data.

Flaw formation in LPBF results from evanescent, multi-scale thermal phenomena extending from meltpool-level (100 μm) to part-level (> 1 mm). Therefore, LPBF process monitoring requires acquisition of data from heterogenous sensors continuously over a long period at high sampling rates. For example, in this work, meltpool temperature data is acquired at a sampling rate of 200 kHz. Hence, LPBF sensor data have all the hallmarks of the 3V's of big data – variety, volume, and velocity.

After acquisition, the sensor signatures are transferred to a data analysis procedure trained to detect flaw formation [36]. There is an inherent latency associated with the transfer and analyses

of the large volume of heterogeneous sensor data despite using high-performance computing and pre-trained models. This latency in detecting incipient flaw formation can potentially exceed the time to recoat and process a layer with fresh powder (typically about 30 to 60 seconds). This latency in the data transfer-analyses loop makes purely data-driven analysis too slow to detect and correct a flaw before it is permanently sealed in by the next layer.

(2) Data-driven models lack generalizability as they do not encapsulate the process physics.

As explained in Sec. 1.1, the thermal history is a function of multiple interlinked factors, such as part geometry, part location, orientation (build layout) and process parameters. For example, in practical LPBF builds, such as those in this work, the cross-section of the part may not be constant, but vary considerably along the build direction (z-direction). The changing cross-section entails that the time to scan a layer also varies from layer-to-layer, which in turn affects the part thermal history and the observed sensor signatures [22, 44]. Accordingly, data-driven approaches trained based on sensor signatures obtained from simple shaped uniform cross-section test coupons, such as cubes and cylinders, may not be generalizable to complex, practical part shapes.

Apart from part shape, the sensor signatures are also contingent on the build plan. For example, if the build plan is modified, e.g., by adding (removing) some parts from the build plate, changing the orientation of parts, altering the scanning pattern, it not only changes the thermal history, but also influences the related sensor signatures [26]. Hence, data-driven models that do not account for the causal thermal physics of the LPBF process are liable to cause significant flaw detection errors when transferred to different build plans even with the same part shape and materials.

(3) ***Data sets in LPBF are expensive to obtain and curate.***

While data-driven machine learning models have been used for flaw detection in LPBF, these models require a relatively large volume of paired input-output observations (labeled data) [36,

43]. Such data is prohibitively expensive to acquire, given the small batch sizes and high cost of raw (powder) materials of LPBF [38]. Moreover, to provide sufficient labeled inputs to build data-driven models, a considerable LPBF-processed parts need to be examined for flaws using non-destructive analysis (e.g., X-ray computed tomography) and microstructural analysis (e.g., scanning electron microscopy) which are laborious, and cost and time prohibitive [22, 42].

1.3 Novelty

In this work we develop and apply a digital twinned, physics and data integrated strategy for detecting incipient flaw formation in LPBF parts as an alternative approach to purely data-driven process monitoring. The key idea of this *digital twin of additive manufacturing* concept as explained in the emerging AM literature (Ref. [33-36]) is to detect part characteristics, such as flaw formation (porosity and deformation), and microstructure evolved by combining theoretical predictions of certain process phenomena derived from a mechanistic (physics)-based model with in-situ process signatures. A mechanism to link the physical predictions and sensor data is through data analytics and machine learning algorithms.

We demonstrate that flaw formation is detected by complementary (twinning) macro-scale part-level thermal history predictions obtained from a physics-based model with meltpool-scale temperature acquired from in-process sensors. In this work, the physics-based model captures the effect of part geometry on the thermal history, and the sensor data acquire local meltpool-level temperature not provided by the physical model. We eschewed simulation of meltpool behavior as it requires considerable computation effort compared to prediction of part-level thermal history. This is because, meltpool-level simulations must account for complex thermal, fluid flow, and surface tension interactions [14, 16, 45]. In contrast, at the part-level, flaw formation is predominantly related to thermal effects.

In this work, the meltpool-level phenomena is captured using a commercial sensing array consisting of multiple photodetectors. The part-level temperature distribution is simulated using the graph theory-based thermal modeling approach. As demonstrated in our prior work, the graph theory approach provides significant computational efficiency-related advantages over finite element-based models in the prediction of the thermal history in LPBF [22, 44, 46-48].

The uniqueness of the digital twin implemented in this work is that the meltpool sensor data is used as a direct input to the graph theory-based thermal model in lieu of applying data-driven models to make the correlations between thermal history predictions, sensor data and part quality [49]. The meltpool temperature measurements acquired in-situ inform (update) the thermal model layer-by-layer during the process as the part is being printed. By combining simulation and sensor signatures, the approach eschews the need to transfer sensor signatures to a separate data analysis algorithm. The approach thus mitigates the detection latency involved in data-driven flaw monitoring. Moreover, since the digital twin incorporates both the macro-scale effect of part shape on thermal history and micro-scale effect of laser-material interaction in the form of the meltpool temperature it inherently encapsulates the effect of different processing parameters, such as scanning pattern, hatch spacing, laser power, velocity etc.

To the best of the authors' knowledge, updating physical model predictions layer-by-layer with in-process sensor signatures in the context of flaw detection in LPBF has not been reported previously. We apply the concept of the digital twin for detecting the onset of three different types of flaw formation pathways in LPBF of complex stainless steel (316L) impeller-shaped parts. The three types of flaw formation pathways studied in this work are: (1) porosity and microstructure heterogeneity due to abrupt change in processing parameters, (2) deliberate embedded voids, and (3) machine anomalies (lens delamination).

The rest of this paper is organized into four sections as follows. Section 2 details the experimental procedure (Sec. 2.1) and sensing array (Sec. 2.2), and describes the digital twin approach combining thermal simulations with in-process sensor data to detect flaw formation in LPBF (Sec. 2.3). The results and conclusions are reported in Sec. 3 and Sec. 4, respectively.

2 Methods

2.1 Experiments

2.1.1 Test Parts and Processing Conditions

As exemplified in Figure 2, four identical stainless steel (SAE 316L) impeller-shaped parts each of diameter 60 mm and height 16.9 mm (Φ60 mm × 16.9 mm) consisting of 845 layers (20 μm thickness) were built simultaneously on an EOS M290 LPBF system. The build time for completing the four impellers is approximately 16 hours and 30 minutes.

The impeller was chosen as an exemplar part to demonstrate the digital twin due to its practical nature. It is divisible into three distinctive regions along the build direction: base, mid, and fin-sections. These sections include complex, challenging to build features such as a teardrop-shaped internal cooling channel, and several inclined thin cross-section fin structures. Given the variation in cross-section along the build height, the surface area scanned by the laser would change from layer-to-layer. Consequently, as is explained in depth in Sec. 2.1.3, the cooling time between layers would vary, and is anticipated to result in a complex thermal history.

A summary of the process conditions is presented in Table 1. The nominal parameter sets were based on *a priori* optimization for SAE 316L alloy suggested by the machine tool manufacturer and based on our recent published work with an identically shape large-scale Φ155 mm × 35 mm impeller reported in Ref. [44]. The metal powder was sourced from Praxair Surface Technologies under the trade name TruForm 316 with mean particle size of 30 μm.

The parts are placed staggered along the diagonal of the build plate for three reasons [50]: (i) to accommodate all four impellers with sufficient spacing between each part (the build plate is 250 mm × 250 mm); (ii) staggering prevents the recoater from encountering all four parts at once, and thus reduces the axial load on the recoater; and (iii) staggering prevents debris and flaws from cascading onto other parts.

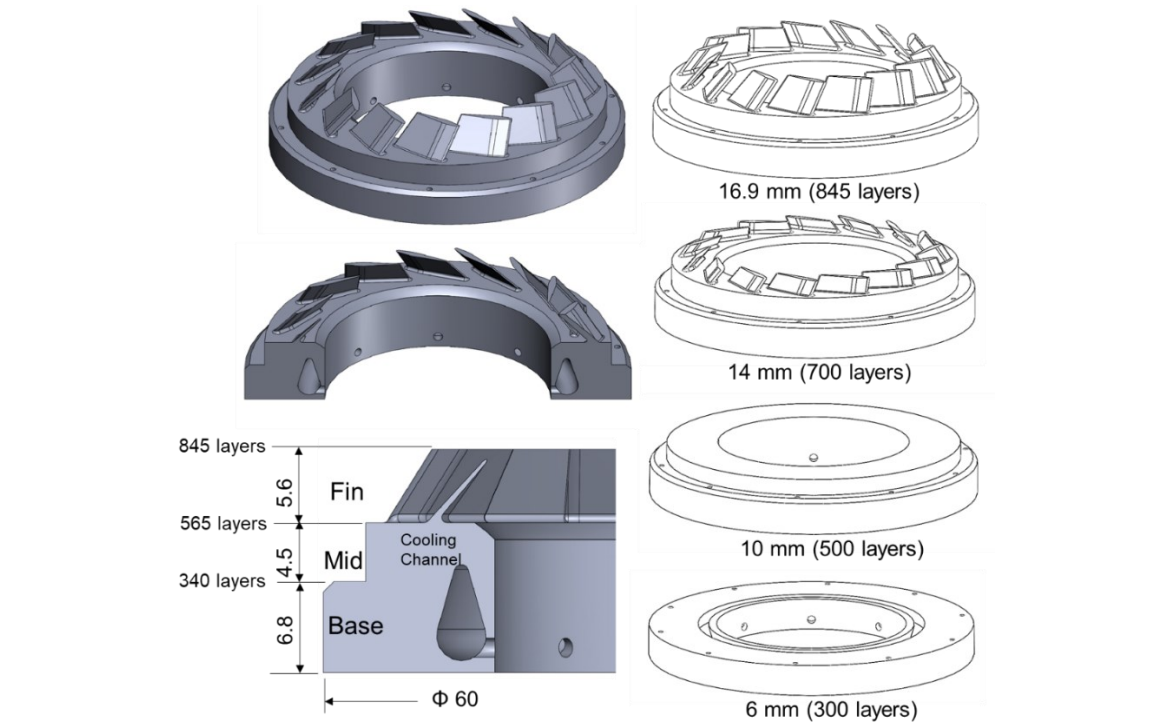

Figure 2: (Top) Cross section of an impeller showing the three build sections: base, mid, and fin. The cooling channel located in the base and mid-section also visible. (Bottom) A representative impeller resulting from the work, and the build layout.

2.1.2 Build Plan

The build plan was devised to initiate three types of flaw formation mechanisms, these are:

(a) Case I: Flaws resulting from changes in processing parameters. These are termed *process drifts* due to deviations in critical parameters, such as laser power from optimized set point.

(b) Case II: Flaws of varying sizes that are deliberately placed in certain sections of the part to emulate cyber intrusions.

(c) Case III: Flaw formation due to a faulty machine. Specifically, processing with a degraded optical coating of the f-θ focusing lens (*lens delamination*).

(a) Case I – Process Drifts (Deviations)

In Case I, as shown Figure 3, the four impeller parts were built under varying laser power settings at different layers to cause flaw formation. For example, for the part labeled Impeller I shown in Figure 3, the laser power was fixed at 195 W (volumetric energy density, E_v ~100 J·mm^{-3}) throughout the build. Impeller I is considered the flaw-free standard or baseline part produced under acceptable conditions and is hereby termed the *Nominal* part. The conditions for the nominal Impeller I are similar to those for an identical larger scale impeller reported in our previous work Ref. [44].

The base and mid-sections of Impeller II were produced at the nominal laser power of 195 W (E_v ~100 J·mm^{-3}), while the fin section was produced under a reduced laser power of 125 W (E_v ~ 64 J·mm^{-3}), viz., a decrease of ~35% in laser power (energy density). Impeller II is termed as processed under *Nominal-Lo* laser power settings. The reduction of the laser power from 195 W to 125 W during processing of the fin region was expected to result in lack-of-fusion porosity due to insufficient material consolidation [42].

Impeller III was produced under *Nominal-Hi* conditions with the base and mid sections processed at laser power 195 W, and the fin section produced at 265 W (~136 J·mm^{-3}), i.e., an increase of ~35% in laser power. Since the fin has the thinnest cross-section, the increase in the

laser power was expected to cause excessive heating leading to grain coarsening in the fin section. Impeller IV termed *Lo-Lo* was produced entirely at a low-level of laser power of 125 W, and was anticipated to result in lack-of-fusion flaw formation throughout its structure.

Table 1: LPBF Process parameters used for building the four impeller-shaped parts in this work on the EOS M290 LPBF machine.

Process Parameter	Values [units]
Laser power (P)	Varies per part (see Figure 3)
Scanning Speed (v)	1083 [mm·s^{-1}]
Hatch spacing (h)	0.09 [mm]
Layer thickness (d)	0.02 [mm]
Stripe overlap	0.12 [mm]
Stripe width	5 [mm]
Scanning strategy	Island scanning (EOS M290 standard)
Build atmosphere	Argon
Build plate Preheat temperature	110 °C
Material Properties	Values [units]
Material type, Praxair TruForm 316	SAE 316L, 30 µm mean Particle size
Oxygen level (maximum threshold)	<10,000 [ppm]

(b) Case II – Flaws Formation due to Cyber Intrusions.

The aim of Case II is to emulate cyber-physical intrusions. Such intrusions can be caused my malicious actors either by placing flaws in the part during the design phase or tampering with the process when the part is being produced [30, 32]. Accordingly, spherical-shaped voids were embedded in Impellers II, III and IV. Figure 4 details the location and relative size of these planted flaws; 52 spherical voids of diameters ranging from Φ 0.03 mm to Φ 0.5 mm were created in each impeller. These dimensions were chosen to represent the typical lack-of-fusion flaw formation in LPBF [5]. There were 13 embedded voids in each quarter sector (quadrant) of the impeller. Voids were created by switching the laser off.

(c) Case III – Flaw Formation due to Machine Faults (Lens Delamination)

Case III emulates flaws caused due to machine faults. In this work we study a particular type of machine flaw called lens delamination, which results from degradation of the optical coatings

on the f-θ lens of the LPBF machine, and subsequently creates an anomaly in the focusing of the laser in two corresponding regions Impeller III. In LPBF machines, the f-θ lens is frequently cleaned and replaced after a certain number of duty cycles as its performance degrades. Factors such as soot agglomeration and ejecta from the process can coat the window of the f-θ lens [9, 51]. Anomalies in the laser focus on account of chromatic aberrations in the f-θ lens are reported by Thombansen *et al.* [52]. The test parts in this work were produced with a damaged optical coating on f-θ lens, which affected laser focus at two specific surface regions of Impeller III (described in Figure 27, Sec. 3.3.3). The inconsistent laser focus due to lens delamination were linked to formation of lack-of-fusion flaws.

Lastly, in closing this section, we note that in LPBF the relative positions of the part on the build plate effects flaw formation and the process signatures [26]. In this work, the foregoing effect is controlled by producing the base region of Impeller I, II, and III under identical conditions. Further, parts were examined with X-ray computed tomography analysis to affirm that flaws were not created due to positional effects.

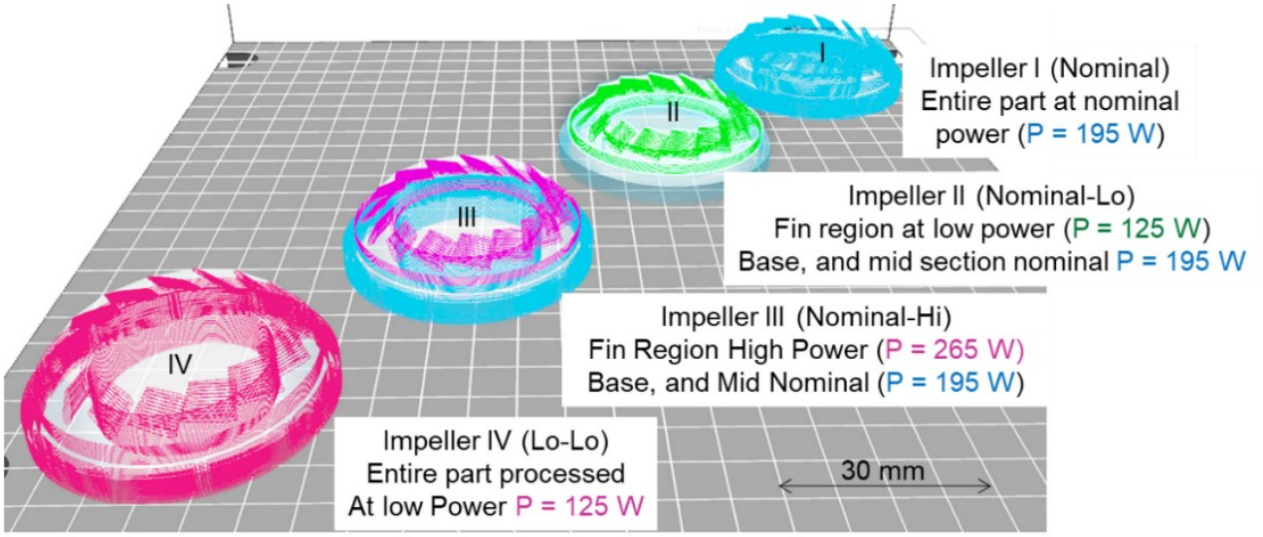

Figure 3: Case I - four impellers are produced under different laser power conditions to mimic the effect of process drifts

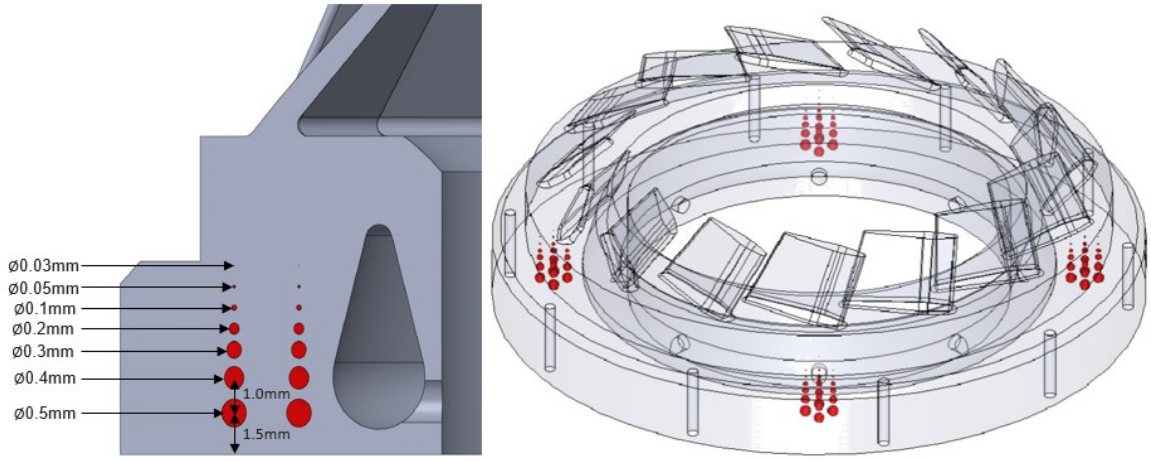

Figure 4: Case II – Voids are embedded into impellers II, III, IV to emulate cyber-physical intrusions. There are total 52 voids planted in a part; 13 spherical-shaped voids are embedded in each quadrant sector of the impeller. The voids have of diameter varying from Φ0.03 mm to Φ0.5 mm by switching off the laser power.

2.1.3 Time between layers (TBL)

An important consideration in LPBF is the time between layers (TBL), which is the cycle time elapsed between the melting of two consecutive layers. The TBL, also called inter-layer time, is a function of the laser velocity, scanning pattern, the surface area of a layer scanned by the laser, and the layer recoating time [22, 26]. The layer recoating time was maintained constant at 10 seconds in this work.

The TBL influences the thermal history of the part. A longer TBL allows for a longer cooling time between layers, which in turn influences the microstructure evolved and thermal-induced residual stresses [22, 26]. In other words, the TBL is coupled to the physical properties of the part. Moreover, the TBL must be accurately estimated before printing the part as it is a critical input to the part-level simulation model used in this work [22]. The TBL was estimated before the build from a slicing software simulation (akin to a G-code emulator).

Figure 5 presents the TBL values for Impeller I as a function of the layer height. The TBL was identical for all four impellers. Due to the variable cross section of each layer, the TBL is not constant, but changes from layer to layer. In this work, the surface area of the impeller scanned by

the laser decreases with the build height and therefore there was a reduction in the TBL with layers, as shown in Figure 5.

Three distinct phases are observed in the TBL corresponding to the three sections of the parts – base, mid and fin. In addition, several momentary peaks caused by upskin and downskin contour finishing parameters are observed. Herein, upskin surfaces refer to regions where unmelted powder exists above a layer. Conversely, downskin layer are those which have unmelted powder below. Typically, upskin and downskin regions in LPBF are processed at a reduced velocity compared to the bulk of the part to improve the surface finish.

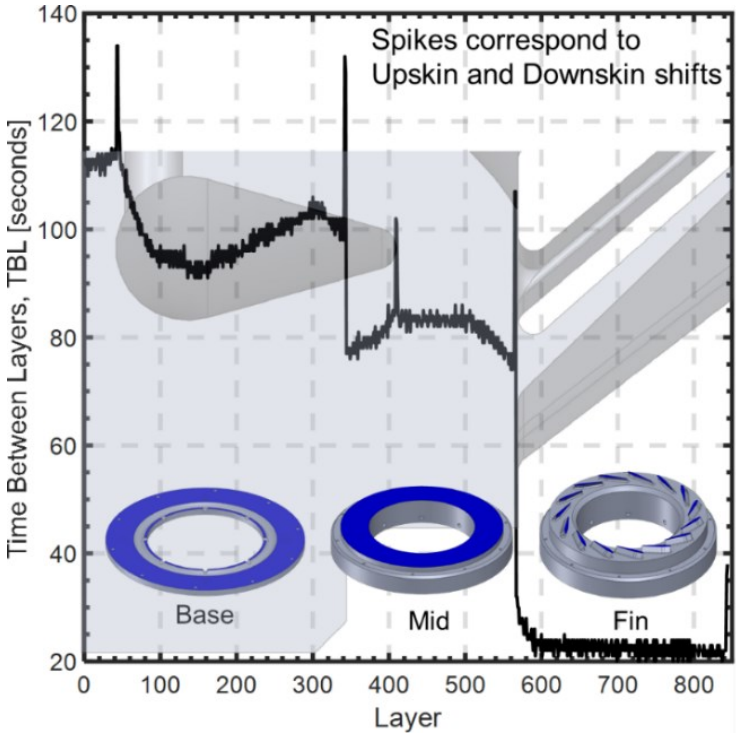

Figure 5: The time between layers (inter-layer time) of the test parts estimated from the slicing software.. The time between layers reduces during the build in proportion to the surface area scanned. The fin-section has the smallest surface area, and hence the laser requires the least time (less than 5 seconds) to scan layers in the fin region. The time to recoat a layer is not included in this plot. The recoat time is constant at 10 seconds per layer.

2.1.4 Post-process characterization

The nature and severity of flaw formation for each of the four impellers resulting from the aforementioned three cases are quantified and characterized through X-ray computed tomography (XCT) and metallurgical analysis. These are described in In Sec. 2.3.3. The XCT analysis allows estimation of the location, distribution, severity, and size of flaw formation inside the part in a non-destructive manner. Subsequent to XCT, each impeller was cross-sectioned, polished and etched for materials characterization. The characterization included optical microscopy (microstructure and type of flaw), scanning electron microscopy (surface texture), and electron backscatter diffraction (evaluate size and orientation of grains).

2.2 In situ Monitoring

2.2.1 Sensing Array

A schematic of the on-axis sensing system integrated into an EOS M290 LPBF system is provided in Figure 6. The sensing array consisted of three photodetectors that were instrumented coaxial with the laser path [53, 54]. This system work had a Lagrangian reference frame measurement, as the sensor observations are obtained by following the meltpool, as opposed to a stationary or Eulerian reference frame in an off-axis sensor where the meltpool moves across the field of view of the sensor [11].

The sensor array was designed to measure the spectral emissions from the meltpool region. The spectral emissions from the meltpool were correlated to the meltpool temperature. Two types of process signatures were derived from the three photodetectors. The first metric, termed *Thermal Energy Planck* (TEP), and the second metric is termed as *Thermal Energy Density* (TED). The key difference in the TEP and TED signatures results from the use of optical filters.

To explain further, the TEP measures the ratio of the signal intensities of two photodetectors equipped with band-pass filters close to the infrared spectrum. The wavelength of the two

photodetectors were 650 ± 5 nm (λ_1) and 700 ± 5 nm (λ_2). These bandpass frequencies are chosen with respect to the peak spectral radiance obtained from Planck's law and the photodetectors peak responsivity. The measured intensities at these two respective frequencies are labeled $S_{\lambda 1}$ and $S_{\lambda 2}$.

Specifically, the TEP = $\log_{10}(S_{\lambda 1}/S_{\lambda 2})$. Since, the temperature of a body is proportional to radiated intensity, the TEP measurement is proportional to the temperature of the meltpool region, with material emissivity as the proportionality constant. However, the material emissivity is not a constant, but depends on the surface roughness and temperature of the body [40]. Hence, using the ratio of the intensities in the TEP signatures at two different wavelengths has the effect of canceling the effect of material emissivity.

The underlying physics of the TEP metric is summarized in the context of Figure 7. The TEP signatures are akin to optical emission spectroscopy measurements detailed in recent works by Nassar *et al.* as they capture radiant energy corresponding to specific wavelengths in the electromagnetic spectrum [55-57]. As explained in Figure 7, as a material is heated, its electrons transition to a higher energy state. On returning to its previous (lower) energy state, the electron emits a photon. The wavelength of the photon (λ) released is in accordance with the Planck-Einstein relationship $E = hc\lambda^{-1}$. The photodetectors from which the TEP signature is obtained are bandpass filtered to detect these emissions resulting from material fusion within a specific frequency (wavelength) range. The intensity of these radiated emissions is directly proportional to the temperature of the heated body. The TEP signature captures variations in the meltpool temperature.

The third photodetector, from which the TED signature was obtained does not filter the optical emissions and captures the broadband radiation from the return path of the laser. The TED metric, represents the data acquired by a third photodetector which does not have an optical band pass

filter, and hence captures emissions over the visible to near-infrared range of the electromagnetic spectrum [41]. The TED metric is intended to detect the broadband energy emissions from the meltpool region.

The TEP and TED measurements are acquired continuously throughout the build at a sampling rate of 200 kHZ and 100 kHz, respectively. For the laser scan velocity of ~1083 $mm \cdot s^{-1}$ used in this work, approximately 200 TEP and 100 TED readings were acquired per millimeter length scanned by the laser. Data acquisition was initiated at the start of a layer, and each sample measurement was correlated to the build location based on the location feedback from the laser Galvano-mirror, i.e., the location where the meltpool senor data is acquired is registered to the position of the laser.

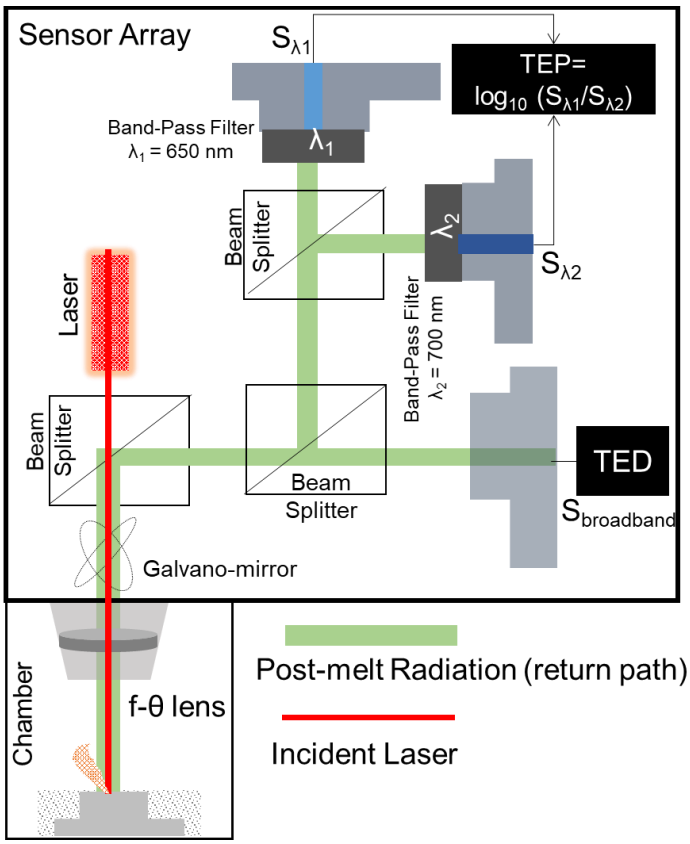

Figure 6: Schematic of the on-axis sensing setup instrumented on an EOS M290 LPBF system. The system consists of three photodetectors. Two photodetectors are bandpass filtered and used to obtain a signature termed Thermal Energy Planck (TEP). The third photodetector, which is not filtered, is used to measure the broadband emission from the chamber termed Thermal Energy Density (TED).

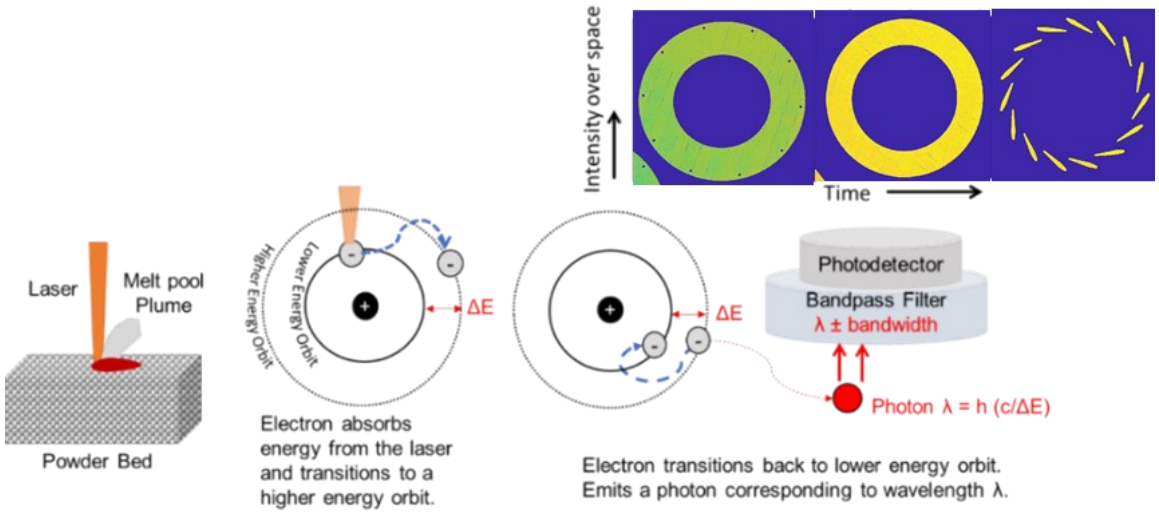

Figure 7: Concept of measuring the meltpool temperature using emissions from a bandpass-filtered photodetector.

2.2.2 Sensor Calibration

We note that the sensor array used in this work does not provide an absolute temperature reading and must be calibrated with a known temperature source. Calibration of the sensor signatures was performed using a tungsten ribbon filament strip lamp. The lamp was first compared to a NIST traceable source between 800 °C to 2,300 °C. The lamp was then installed within the LPBF machine with the laser galvanometers aligned to have the lamp centered within their field of view. Using a controlled power source, the lamp was brought to temperature setpoints between 800 °C and 2,300 °C in 100°C increments. For each temperature setpoint an in-process measurement with the sensing system was performed.

In Figure 8 the setpoint of the tungsten strip lamp is plotted as a function of the observed TEP signature for three independent replications. As noted in Sec. 2.2.1, concerning the y-axis of Figure 8, TEP = $\log_{10}(S_{\lambda 1}/S_{\lambda 2})$, where $S_{\lambda 1}$ and $S_{\lambda 2}$ are the intensities acquired by the two photodetectors at $\lambda_1 = 650$ nm and $\lambda_2 = 700$ nm. Thus, a relationship was obtained which showed that the TEP measurement is proportional to the surface temperature ($R^2 \sim 99\%$). This relationship serves as the basis for normalizing the TEP signatures into an absolute meltpool temperature between 1800 °C

to 2300 °C. This meltpool temperature range is observed in the LPBF of stainless steel 316L [58]. Given the broadband nature of the TED signature, and because the effect of emissivity is not negated, conversion of the TED to an absolute temperature is not appropriate. In closing this section, we note that the calibration was done with a black body radiation reference source (tungsten filament strip lamp). As the TEP measurements are calibrated in the absence of an actual part and powder material, hence, we eschewed conversion of TEP measurements to absolute temperature. In our future works we will calibrate the TEP measurements to an absolute temperature scale by calibrating the sensor array with an actual build.

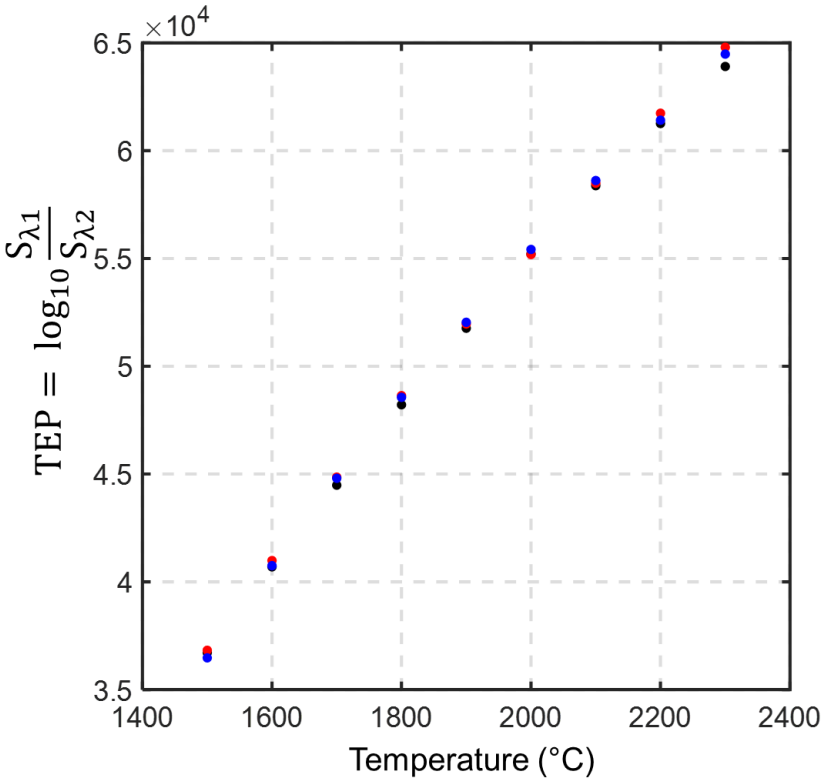

Figure 8: Curve relating TEP = $\log_{10}(S_{\lambda 1}/S_{\lambda 2})$ vs. temperature setpoints on the tungsten strip lamp signatures for three replications. The TEP is directly proportional to the absolute temperature (R^2~ 99%). The calibration curve is reported for three independent replications.

2.2.3 Data Sampling and Representative Measurements

The TEP and TED measurements were acquired continuously throughout the build at a sampling rate of 200 kHZ and 100 kHz, respectively. An example of the TEP sensor measurements, consolidated in terms of 2D color-scaled images for layers 60 (1.2 mm), 450 (9 mm), and 750 (15 mm) of the build is shown in Figure 9. The representative data for Impeller I from layer 1 to 720 in steps of 90 layers is shown in the first three rows of Figure 9. The resolution of the data is close to 125 μm × 125 μm per pixel image. Figure 9(bottom row) shows the TEP data consolidated for all four impellers. The occurrence of lens delamination in Impeller III is evident in the bottom row of Figure 9 demarcated by the cold spots in the north-west and south-east quadrants of Impeller III.

To obtain a temporal (1D) trend of sensor data as a function of time, the TEP and TED signatures were sampled for specific spatial regions of the part shown in Figure 10. The measurements at these regions were used as inputs to the graph theory approach. In practice, several hundred such critical regions of the part can be sampled and monitored in parallel, without sacrificing computational efficiency, as the graph theory approach simulates the thermal history for the entire volume of the part. In this work, temperature data over three types of locations were sampled: (i) locations without any artificially planted flaws, (ii) locations where flaws were planted, and (iii) regions where lens delamination was suspected.

The sampled regions are demarcated in Figure 10(left). The sample area equates to a total of 2 pixel × 2 pixel in terms of the sensor data on the surface of the current layer deposited on the part. This sampled area corresponds to 250 μm × 250 μm consisting of 50 TEP and 50 TED measurements per layer. These measurements with the sampled area were subsequently averaged and a single average temperature readings is presented for the layer. The sample area was selected

to contain the narrow cross-section of the fin. Sampling near the boundaries was avoided to reduce image blurring and resolution-related errors. In the base and mid sections of the impeller, the sample area was held in the same location for each layer. The sample area for the fin was relocated as shown in Figure 10 with each layer to accommodate the changing section of the fin.

The representative TEP and TED signatures acquired in the region without embedded flaws for Impeller I are shown in Figure 11. The temperature, and as a consequence the TEP signature values increase as a function of the build height even though the energy density is held constant due to the following two reasons. First, the time between layers (TBL) as observed in Figure 5 progressively decreases from 120 seconds in the base, to 80 seconds for the base, and finally 20 seconds in the fin section. Hence, there is not sufficient time between layer for the heat to be conducted from the fin region. Second, the cross-section and surface area of each layer in the fin region are considerably smaller than that of the base and mid sections, which exacerbates heat buildup. The resulting uneven temperature distribution with the impeller would lead to microstructure heterogeneity and inconsistent properties [22].

The TED signature, however, does not respond to change in the part shape. The inherent and significant variation in the TEP signature as a function of the build height, despite maintaining a steady process conditions, underscores the importance of accounting the effect of shape of the part, and in a broader context, the fundamental thermal physics of the process when devising flaw detection algorithms.

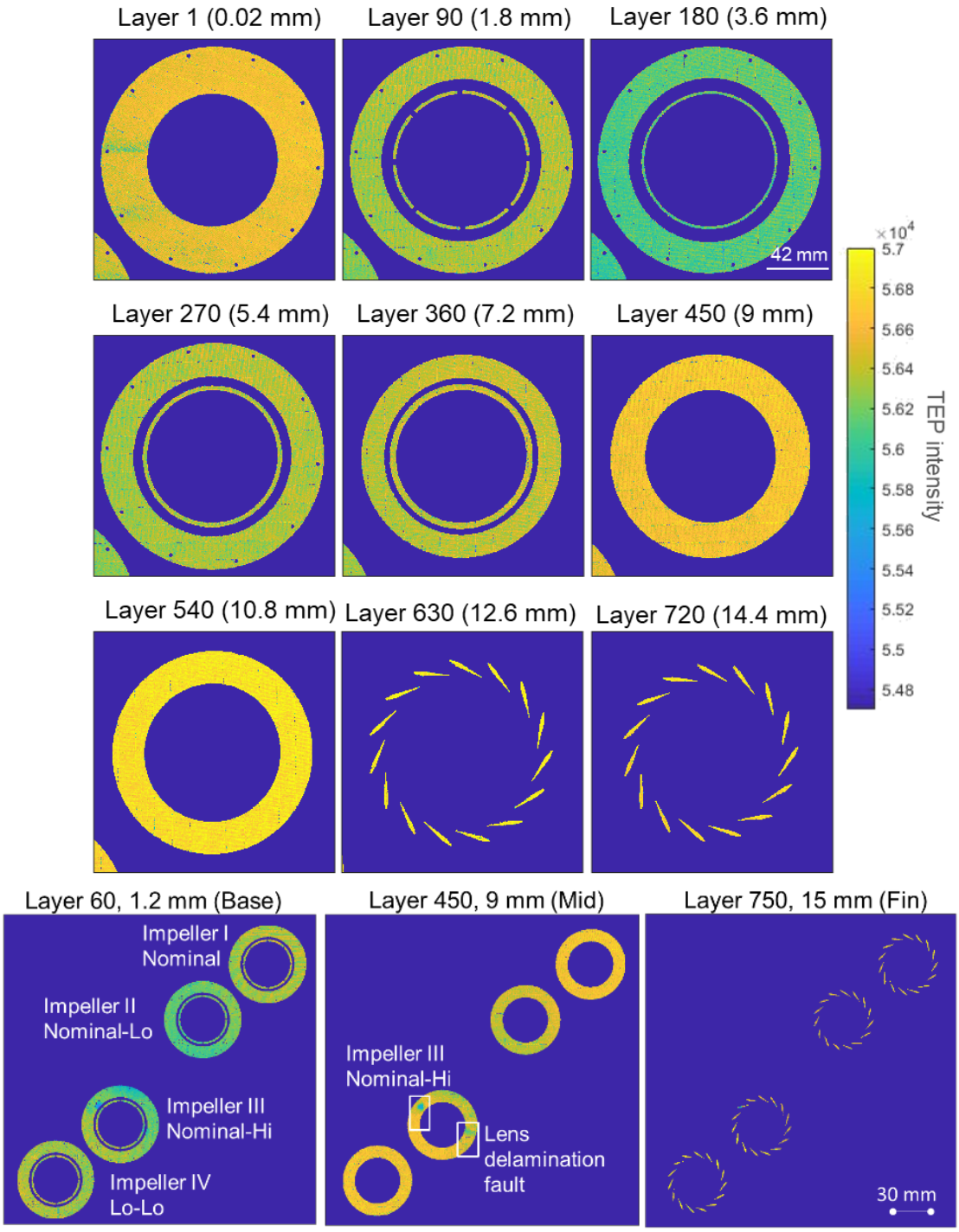

Figure 9: (top three rows) 2D Layer-by-layer TEP measurements for Impeller I following the melting of the layer. (bottom row) TEP measurements compiled for various layers for all four impellers. Lens delamination is observed in Impeller III in the demarcated regions. Due to delamination cold spots are formed, hence, the measured intensity of TEP signatures is reduced. These cold spots can potentially lead to lack-of-fusion porosity.

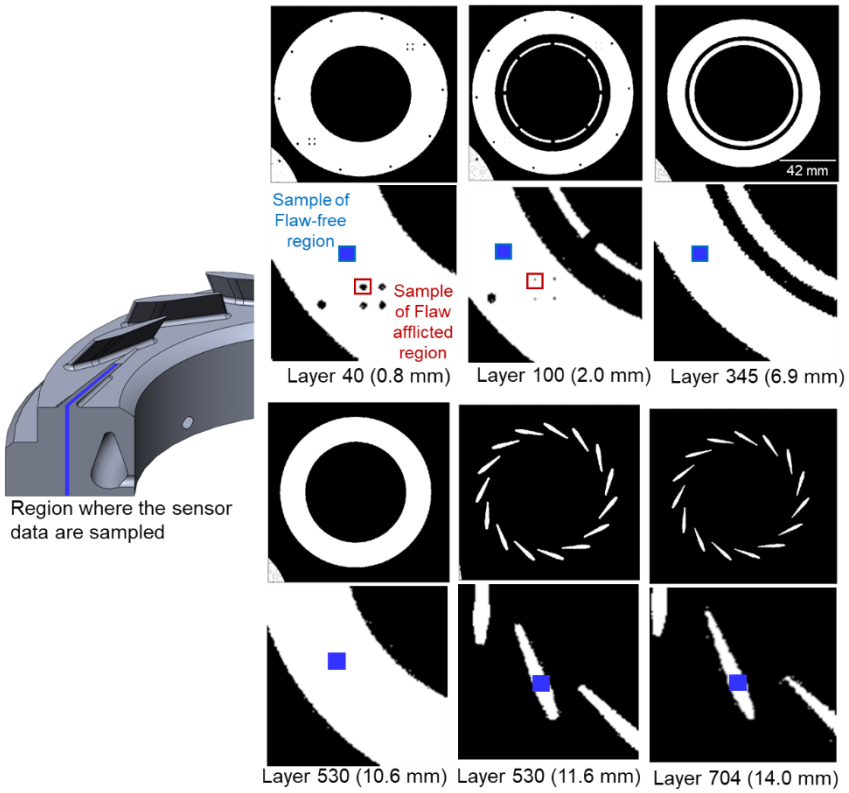

Figure 10: The spatial ragions where sensor data are sampled is demarcated with a blue strip. The sampled area is 2 pixels × 2 pixels (250 μm × 250 μm). Sampled area for regions with embedded flaws are enclosed in red.

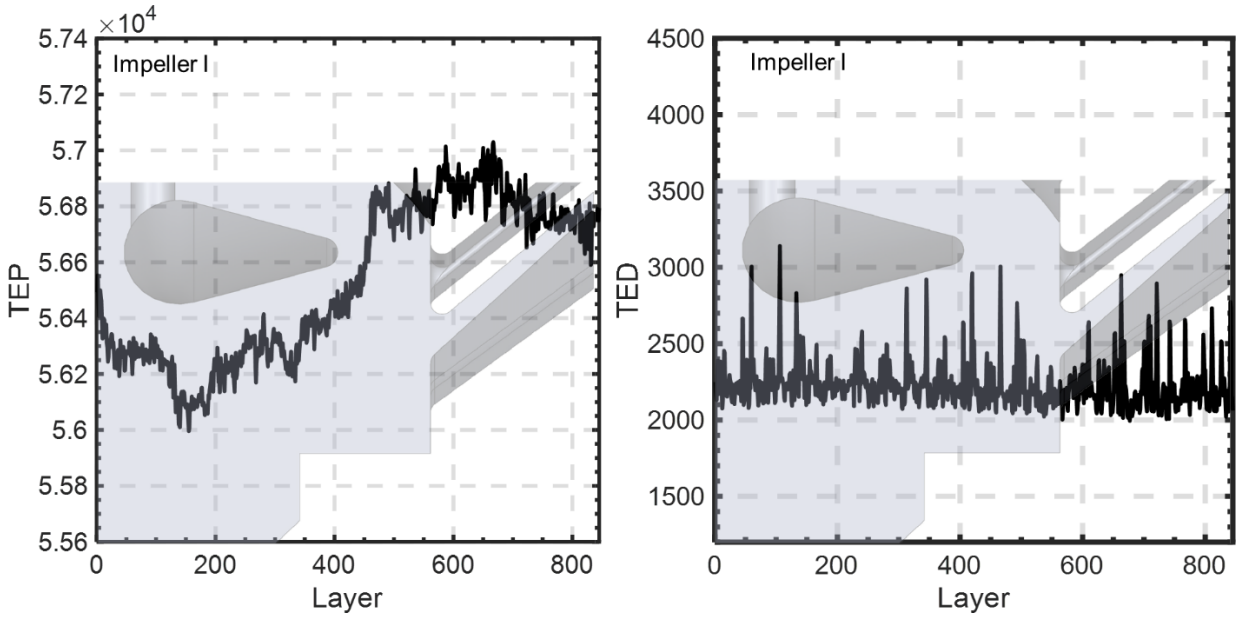

Figure 11: Representative process signatures sampled at locations without embedded flaws for Impeller I. (left) TEP and (right) TED data. The TEP signature increases as a function of the build height. The increase corresponds to the decrease in the TBL shown in Figure 5. The TED signature given its broadbrand nature does not respond to change in part shape.

2.3 The Digital Twin Approach

The realization of the digital twin hinges on seamless integration of two phases, as delineated in Figure 12. These phases are:

- Phase I - *mirror-as-you-build* - using graph theory to predict the thermal history of the entire part before it is printed. The simulation timescale is a fraction of the actual time to print the part (7 minutes vs. 16.5 hours).
- Phase II – *qualify-as-you-build* - detecting flaw formation during the process by updating the thermal history prediction obtained from Phase I layer-by-layer based on in-process sensor signatures (TEP, Sec. 2.2, Figure 11).

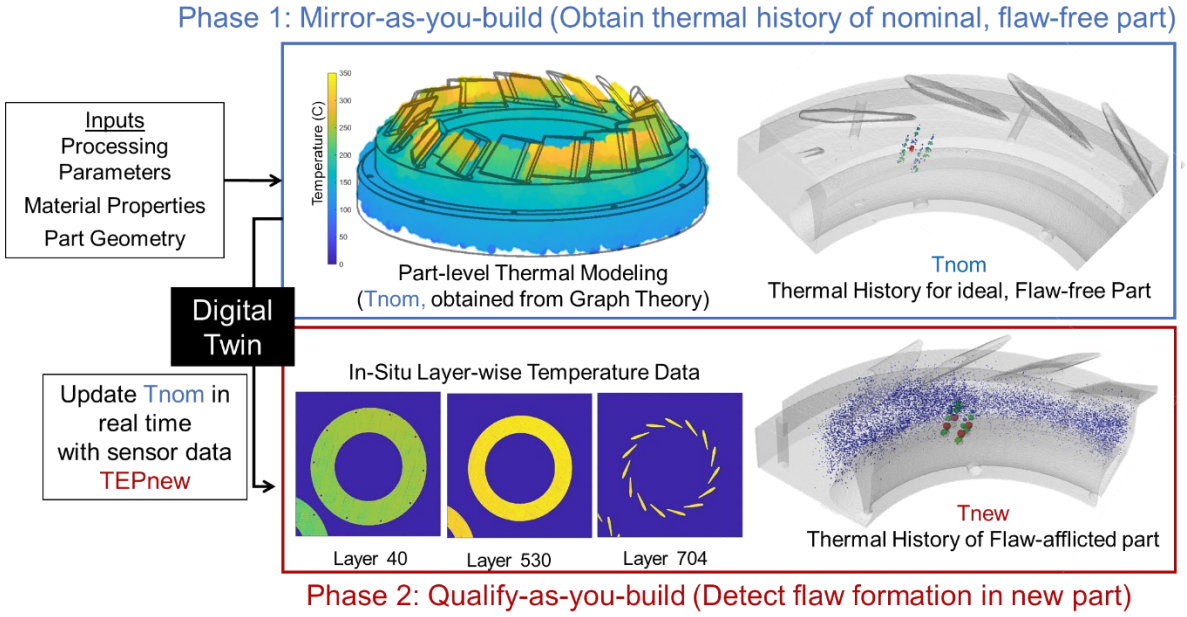

Figure 12: The concept of the digital twin applied to practical impeller-shaped parts. The approaches involves two phase. In Phase I, called the mirror-as-you-build phase, the part-level thermal history for a flaw-free impeller is predicted using a graph theory. In Phase II, the qualify-as-you-build phase, the thermal history of a new part is obtained and monitored by updating the thermal history of a nominal part with in-situ sensor data.

As an analogy with statistical process control, Phase I – mirror-as-you-build – encapsulates the common cause variation by predicting the thermal history of a part in its flaw-free state or nominal state using the graph theory approach and in situ sensor data. The thermal history of the nominal, flaw-free state represents natural variations in the thermal history on account of the changing cross-section of the part along with inherent stochastic (white) noise in the process.

In other words, in Phase I, the graph theory model is trained (calibrated) to predict the thermal history of an impeller produced under ideal conditions. In this work, Impeller I represents the flaw-free or nominal condition. Thus, Phase I predicts the layer-by-layer thermal history of Impeller I represented as $T_{nom}(l)$ for each layer l. The corresponding meltpool temperature for the layer l for Impeller I is obtained from the TEP signature, labeled $TEP_{nom}(l)$, is incorporated into the graph theory model.

Phase II, called qualify-as-you-build, is intended to detect flaw formation in a new part (of a similar shape). Phase II therefore captures special cause variation in the process which are indicative of impeding flaw formation. In Phase II, the layer-by-layer thermal history of a new part $T_{new}(l)$ is predicted by instantaneously updating the thermal history of the nominal condition $T_{nom}(l)$ based on its corresponding layer-by-layer TEP and TED signatures $TEP_{new}(l)$ and $TED_{new}(l)$, respectively. In this work the new part is represented by Impellers II, III, and IV. A process drift, symptomatic of an incipient flaw is indicated if the thermal history of a new part $T_{new}(l)$ deviates considerably from the thermal history of the nominal flaw-free Impeller I, $T_{nom}(l)$. Each of the two phases is discussed in detail herewith.

2.3.1 Phase I – Mirror-as-you-build

(a) Background - The Graph Theory Approach for Thermal Modeling in LPBF

The thermal aspects of the LPBF encompass conductive, convective, and radiative heat transfer across three scales, namely, meltpool scale (< 100 μm), meso-scale track-level (100 μm – 1 mm), and part-scale (> 1 mm) [14, 16, 17]. It is computationally cumbersome to capture effects from all three scales within a single model. Particularly, meltpool modeling in LPBF is exceedingly time consuming and requires high performance computing [14, 17]. In this work the part-level thermal history is modeled using graph theory, while the meltpool-level phenomena is observed through the TEP and TED signatures.

To predict the part-level thermal history it is necessary to solve the *heat diffusion equation* [59] as written in (1),

$$\overbrace{\widetilde{\rho c_p}}^{\substack{Material\\ Properties}} \frac{\partial \mathrm{T}(x,y,z,t)}{\partial t} - k\overbrace{\left(\frac{\partial^2}{\partial x^2}+\frac{\partial^2}{\partial y^2}+\frac{\partial^2}{\partial z^2}\right)}^{Shape\ of\ the\ Part}\mathrm{T}(x,y,z,t) = \overbrace{\frac{\mathrm{P}}{\mathrm{v}\times\mathrm{h}\times\mathrm{d}} = \mathrm{E}_V}^{Parameters} \tag{1}$$

here T is the temperature rise above the ambient temperature.

The accompanying initial and boundary conditions are given by,

$$\mathrm{T}(x,y,z,0) = 0 \text{ (initial condition)},$$

$$\frac{\partial \mathrm{T}}{\partial n} = 0 \text{(on boundary)}. \tag{2}$$

Solving the heat diffusion equation results in the temperature $\mathrm{T}(x,y,z,t)$ at a location (x, y, z) and time instant t inside the part. The energy density [J·m^{-3}], E_V, is the energy needed to melt a unit volume of material and is a function of laser power (P [W]), distance between adjacent tracks of the laser (h) [m], translation velocity (v) [m·s^{-1}], and layer thickness (d) [m]; these are controllable parameters of LPBF. The material properties are density ρ [kg·m^{-3}], specific heat c_p [J·kg^{-1}·K^{-1})], and thermal conductivity k [J·m^{-1}· s^{-1}·K^{-1}]. The part shape is represented in the second derivative term, called the continuous Laplacian.

In the context of LPBF, FE analysis has been used to solve the heat diffusion equation [15, 23, 24, 60-62]. Meshing of the part geometry is the computationally time-consuming aspect of such FE-based thermal analysis in LPBF. This is because the part shape changes continually with deposition of each new hatch or layer and has to be re-meshed. Accordingly, there is an urgent need for approaches that eschew the meshing steps in FE [63-65].

The graph theory approach reduces the computational burden by solving a discrete version of the heat diffusion equation. The resulting graph theory solution to the heat diffusion equation, as explained in our prior work, is given as [22, 44, 46-48],

$$\overbrace{\mathrm{T}(x,y,z,t)}^{\substack{3D\\ Thermal\ History}} = \overbrace{\phi e^{-\alpha\Lambda\tau}\phi'}^{\substack{Part\\ Shape}} \times \overbrace{\mathrm{T}_o}^{\substack{Input\\ Temperature}} \tag{2}$$

Eqn. (2) entails that the heat diffusion equation is solved as a function of the eigenvalues (Λ) and eigenvectors (ϕ) of the Laplacian Matrix (L), constructed on a discrete set of nodes. Also, from Eq. (2), the thermal history can be surmised to be a function of two aspects, the shape of the part represented by $\phi e^{-\alpha\Lambda\tau}\phi'$ and the input temperature T_o. In this work T_o is the meltpool temperature obtained from the TEP signature. The term τ on the exponent is the time between layers (TBL), and $\alpha = k/\rho c_p$. As noted previously in Sec. 2.1.3, in the context of Figure 5, the TBL is not constant, but varies in proportion to the scanned surface area. The TBL was estimated *a priori* to printing using a slicing software. The graph theory approach has the following three advantages over FE-based simulation in LPBF [23, 24].

(1) *Elimination of mesh-based analysis*: The graph theory approach represents the part as discrete nodes, which eliminates the tedious meshing and re-meshing steps required in the element birth-and-death approach typically used in the FE-based thermal analysis of LPBF.

(2) *Elimination of matrix inversion steps*. While FE analysis rests on matrix inversion at each timestep for solving the heat diffusion equation, the graph theory approach uses matrix multiplication, which greatly reduces the computational burden. As will be demonstrated in Sec. 2.3.3, the computation time for the Phase I prediction of the thermal history is less than 7 minutes, which is less than 1% of the actual build time of 16.5 hours.

(3) *Elimination of time stepping*. The time step τ in the exponent of Eqn. (2) can be set to any value, without having to step through (simulate) smaller time instances which requires remeshing in FE [23, 24].

(b) Predicting the thermal history of LPBF parts using graph theory

In this section, we detail the manner in which the graph theory approach is applied for thermal modeling in LPBF. There are five steps in the approach, four of which are summarized in Figure 13. In our previous work we have verified and validated the graph theory approach with finite element, finite difference, exact Green's function analysis, and experimental observations [22, 44, 46-48]. These prior publications show that the graph theory approach converges 5 to 10-times faster than FE analysis, and the predictions are within 5% (mean absolute percentage error, MAPE) of experimental measurements.

The computationally efficient nature of the graph theory approach facilitates computation of the thermal history within $1/10^{th}$ of the time required to build a part. This was recently demonstrated ib a large-scale (Φ155 mm × 35 mm) version of the impeller used in this work [44].. Herewith we provide a brief summary of the approach for the convenience of the reader.

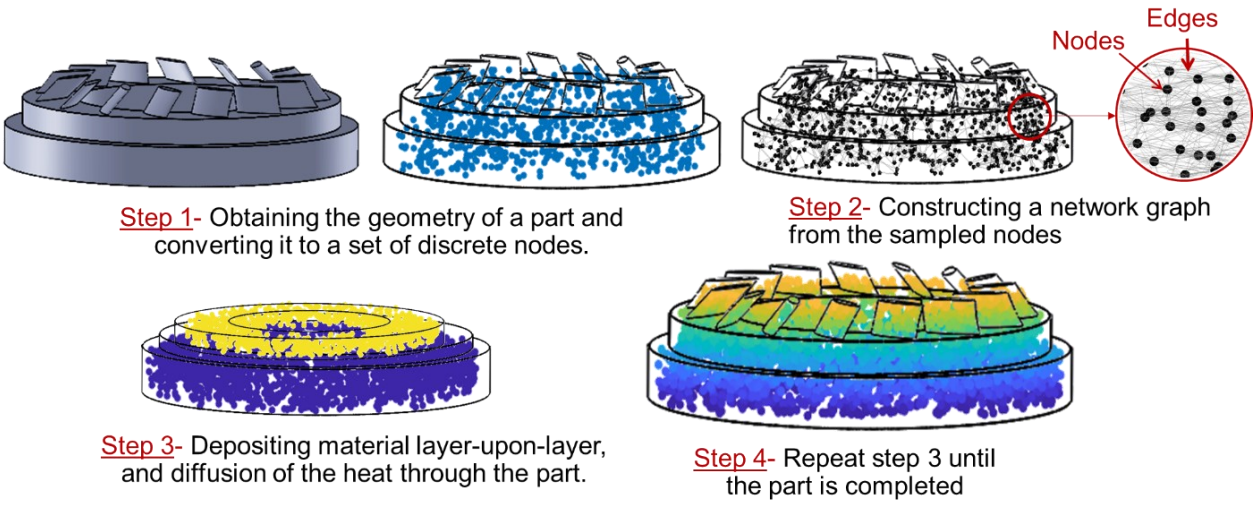

Figure 13: Schematic depiction of four of the five steps in the graph theory approach for predicting the thermal history in LPBF.

Step 1: Convert the entire part into a set of discrete number of nodes (n) that are randomly allocated through the part.

The part is sliced into layers and a fixed number of *n* spatial locations (i.e., nodes) are sampled at random locations in each layer. The position of these nodes is recorded in terms of their spatial coordinates (*x,y,z*). In the ensuing steps, the temperature at each time step is stored at these nodes. The random sampling of the nodes bypasses the expensive meshing of FE analysis and is one of the key reasons for the reduced computational burden of the graph theory approach.

Step 2: Construct a network graph among randomly sampled nodes.

Consider two nodes, π_i and π_j whose spatial Cartesian coordinates are $c_i \equiv (x_i, y_i, z_i)$ and $c_j \equiv (x_j, y_j, z_j)$, respectively; π_i and π_j are connected by an edge whose weight $a_{i,j}$ is given by,

$$a_{i,j} = e^{-\frac{(c_i - c_j)^2}{\sigma^2}}. \quad (3)$$

The edge weight, a_{ij} represents the normalized strength of the connection between the nodes π_i and π_j and has a value between 0 and 1; σ^2 is the variation of the distance between all nodes that are connected to each other. We only connect a node to a certain number of its nearest neighboring nodes. First, we begin by connecting all nodes within a certain Euclidean radius of *l* called the characteristic length. The characteristic length depends upon the thinnest cross-section of the part, and in this work, it corresponds to the thickness of the fin section, $l = 2$ mm.

Next, within the neighborhood of *l,* we only retain edges between the nearest ten nodes ($\eta = 10$). The number of nearest neighbors (η) is calibrated from experiments shown in previous work [44, 48]. From a physical perspective, the edge weight $a_{i,j}$ embodies the Gaussian law – called heat kernel — in the following manner. The closer a node π_i is to another π_j, exponentially stronger is the connection ($a_{i,j}$) and hence proportionally greater is the heat transfer between them.

The matrix, formed by placing $a_{i,j}$ in a row *i* and column *j,* is called the adjacency matrix, $A = [a_{i,j}]$, where N is the total number of nodes.

$$\mathrm{A} = \begin{bmatrix} 0 & a_{1,2} & a_{1,3} & \cdots & a_{1,\mathrm{N}} \\ a_{2,1} & 0 & a_{2,3} & \cdots & a_{2,N} \\ a_{3,1} & a_{3,2} & 0 & \cdots & a_{3,N} \\ \vdots & \vdots & \vdots & \ddots & \vdots \\ a_{\mathrm{N}.1} & a_{\mathrm{N}.2} & a_{\mathrm{N},3} & \cdots & 0 \end{bmatrix} \tag{4}$$

From the adjacency matrix (A), the discrete graph Laplacian matrix L will be obtained using the following elementary matrix operations. The degree of node π_i is computed by summing the i^{th} row of the adjacency matrix A,

$$d_i = \sum\nolimits_{\forall j} a_{i,j} \tag{5}$$

The diagonal degree matrix D is formed from d_i's as follows; where n is the number of nodes,

$$\mathrm{D} = \begin{bmatrix} d_1 & \cdots & 0 \\ \vdots & \ddots & \vdots \\ 0 & \cdots & d_{\mathrm{n}} \end{bmatrix} \tag{6}$$

From the degree of node d_i, the Laplacian l_{ij} at node i is defined as follows:

$$l_{i,j} \stackrel{\text{def}}{=} d_i - a_{i,j} \tag{7}$$

The discrete Laplacian L can be cast in matrix form as,

$$\mathrm{L} \stackrel{\text{def}}{=} (\mathrm{D} - \mathrm{A}). \tag{8}$$

$$\mathrm{L} = \begin{bmatrix} +d_1. & -a_{1,2} & -a_{1,3} & \cdots & -a_{1,\mathrm{N}} \\ -a_{2,1} & +d_2. & -a_{2,3} & \cdots & -a_{2,N} \\ -a_{3,1} & -a_{3,2} & +d_3. & \cdots & -a_{3,N} \\ \vdots & \vdots & \vdots & \ddots & \vdots \\ -a_{\mathrm{N},1} & -a_{\mathrm{N},2} & -a_{\mathrm{N},3} & \cdots & +d_{\mathrm{N}\cdot} \end{bmatrix}$$

Finally, the Eigen spectra of the Laplacian L, is :

$$\mathrm{L}\phi = \phi\Lambda. \tag{9}$$

Step 3: Simulate the deposition of the entire layer and diffuse the heat throughout the network.

To aid computation, the simulation proceeds in the form of a superlayer (metalayer). In this work, we used 10 actual layers each of height 50 μm for one superlayer. The thickness of each superlayer was therefore 0.5 mm. The superlayer thickness is calibrated in Sec. 2.3.3.

The heat diffuses to the rest of the part below the current layer through the connections between the nodes. If the temperature at each node is arranged in matrix form, the steady state temperature T after time t (where t = time between layers, TBL, Figure 5) is obtained as a function of the eigenvectors (ϕ) and eigenvalues (Λ) of the Laplacian matrix (L) of the network graph, viz., Eqn. (2) is repeated herewith, with a tunable parameter called the *gain factor* (g). The gain factor is also set from our previous work with SAE 316L[44, 48].

$$\mathrm{T}(x, y, z, t) = \phi e^{-\alpha g \Lambda \tau} \phi' \mathrm{T}_0. \tag{10}$$

In our previous works, the melting temperature of the material was used as the input temperature T_0 [22, 44, 46-48]. While this steady state approximation is satisfactory for the prediction of the end-of-layer thermal history, however, for flaw detection it is necessary to consider the meltpool-level temperature. In other words, to predict incipient flaw formation the graph theory approach must be modified to accommodate the instantaneous meltpool temperature obtained from the in-process sensor, as opposed to the steady state (constant) material melting temperature [8, 14].

Accordingly, the meltpool temperature obtained from the (calibrated) TEP sensor signatures over sampled region of a layer (l). The TEP is incorporated input the graph theory solution to the heat diffusion equation by substituting $\mathrm{T}_0 = \mathrm{TEP}(l)$ in Eqn. (10),

$$\mathrm{T}_{nom}(x, y, z, t) = \phi e^{-\alpha \Lambda \tau} \phi' \times \mathrm{TEP}_{nom}(x, y, z, t) \tag{11}$$

Setting $\mathbb{S}(l) = \phi e^{-\alpha \Lambda \tau} \phi'$, and the corresponding meltpool temperature $\mathrm{TEP}_{nom}(l)$ the thermal history for layer l of a nominal, flaw free part, $\mathrm{T}_{nom}(l)$, is obtained as,

$$\mathrm{T}_{nom}(l) = \mathbb{S}(l) \times \mathrm{TEP}_{nom}(l) \tag{12}$$

We note that the heat diffusion equation does not account for heat loss due to radiation and convection at the top boundary of the part. Hence, after the temperature of each node is obtained, convective and radiative thermal losses are included for the nodes on the top surface of each layer

in Eqn. (13). Accordingly, we demarcate the nodes at the top boundary, and adjust the temperature of the boundary nodes (T_b) using the lumped capacitive theory:

$$T_b = e^{-\tilde{h}(\Delta t)} (T_{bi} - T_\infty) + T_\infty \quad (13)$$

where, T_∞ (= 300 K) is the temperature of the surroundings, T_{bi} is the initial temperature of the boundary nodes, T_b is the temperature of the boundary nodes after heat loss occurs, Δt is the dimensionless time between laser scans, and $\tilde{h}$ is the normalized combined coefficient of radiation (via Stefan-Boltzmann law) and convection (via Newton's law of cooling) from boundary to the surroundings [66].

Step 4: Step 3 is repeated layer-by-layer until the part is built.

Step 5: Obtaining the instantaneous surface temperature from the simulation.

The thermal history T_{nom} for the nominal, flaw-free impeller Impeller I obtained from Eqn. (12) is depicted in Figure 14(a). The thermal history for one layer is shown in Figure 14(b). These temperature trends are plotted for the flaw-free sampled location shown in Figure 10.

In the cooling curves shown in Figure 14, two distinctive aspects are observed. The first is the transient temperature instantly after the laser strikes the sampled area. The second is the lower temperature reached at the end of a layer (cycle) before the laser returns for melting the next layer.

In this work, once the cooling curve is obtained, the temperature response after 0.1 seconds following the laser strike is extracted. This output temperature, $T_{nom}(l)$, which captures the surface temperature immediately following a laser strike, is called the transient or instantaneous temperature.

The reasoning for selecting the transient (instantaneous) temperature to represent $T_{nom}(l)$, is provided in terms of Figure 15. In Figure 15 the response is plotted for two different time scales following a laser strike. These are 0.1 sec after the laser strike in Figure 15(a), called instantaneous

surface temperature; and after the layer is deposited, called end-of-cycle surface temperature in Figure 15(b). Comparing Figure 15(a) with Figure 15(b), it is evident when the simulation output is sampled at the end-of-cycle temperature, the effect of part geometry on the thermal history dominates, and the local temperature variations are occluded. Since, the local temperature is critical to detect process flaws, therefore, the output temperature obtained 0.1 seconds after the laser strike is chosen to represent $T_{nom}(l)$.

The consequence of using the end-of-cycle surface temperature vs. the instantaneous surface temperature is further visualized in Figure 16 in terms of the three-dimensional temperature distribution obtained from graph theory. The local temperature differences that are evident in the graph theory simulation via the instantaneous temperature T_{nom} are attenuated in the end-of-cycle thermal profile, as the part has had time to cool.

It is noted that the instantaneous temperature in Figure 15(a) significantly exceeds the melting point of stainless steel SAE 316L (~1370 °C to 1500 °C). This is to be expected, because, the meltpool temperature is considerably above the melting point of the material as observed by Hooper *et al.* [58]. Indeed, Khairallah *et al.'s* theoretical simulation indicates that the maximum meltpool temperature in the LPBF of stainless steel exceeds the boiling point [14]. Furthermore, the field of view of the sensing system used in this work captures thermal phenomena in the meltpool region. The meltpool region, apart from the physical meltpool, encompasses the meltpool plume and spatter (ejecta), whose temperatures are observed to exceed the boiling point of the material [67].

In both Figure 15 and Figure 16 it is noted that the surface temperature increases along the build direction, and peaks near the fin region. This is because, the fin region has both the smallest cross-section and the least time between layers (TBL, Figure 5). The TBL reduces to 20 seconds in the

fin region from 120 seconds and 80 seconds for the base and mid sections of the impeller respectively. The reduction in cross-section and smaller time to cool between layers (decrease in the TBL) lead to heat buildup in the fin section.

Although, as shown in Figure 14, the temperature at the instant of the laser strike approaches 2000 °C, the instantaneous temperature T_{nom} in Figure 15(a) and Figure 16 reach a maximum value of 1900 °C due to two reasons. First, the temperature is measured 0.1 second following the laser strike. Second the temperature is averaged over a surface area of 250 μm × 250 μm as explained in Sec. 2.2.3.

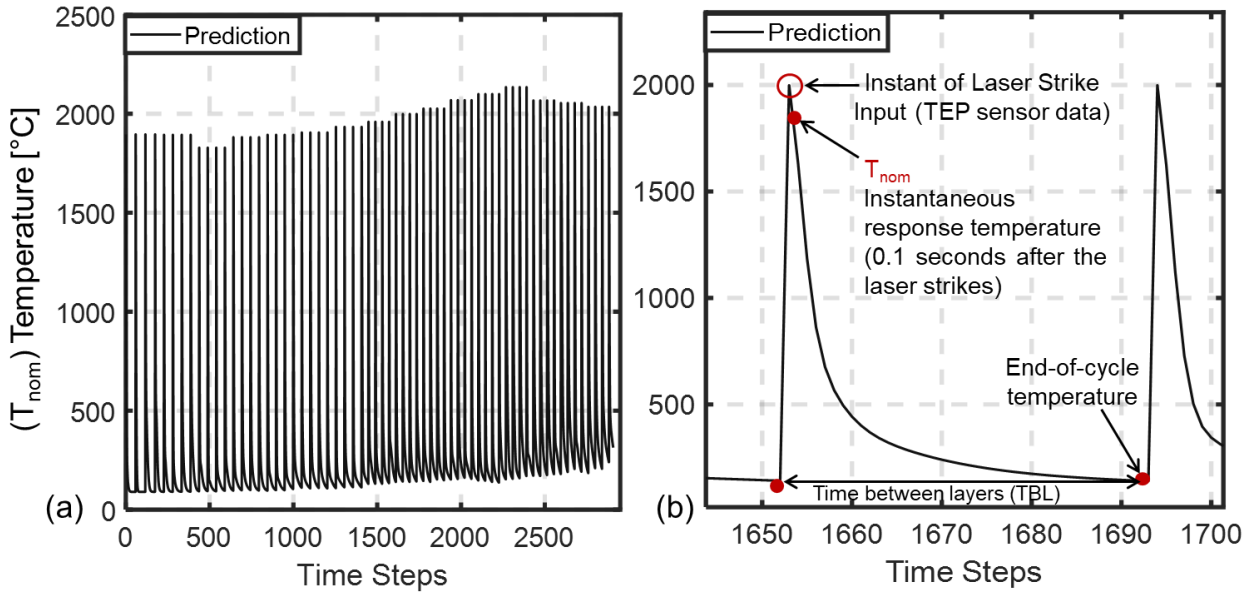

Figure 14: The thermal simulation of the part with input from the TEP sensor, Eqn. (12). (a) The output for the entire 845 layers of part, (b) zoomed-in section of the thermal history, showing the two peaks resulting from the laser strike, and the plateau at the end of a layer (end-of-cycle temperature). In this work, we sampled the simulation output 0.1 seconds after the laser strike, this output is the instantaneous temperature $T_{nom}(l)$.

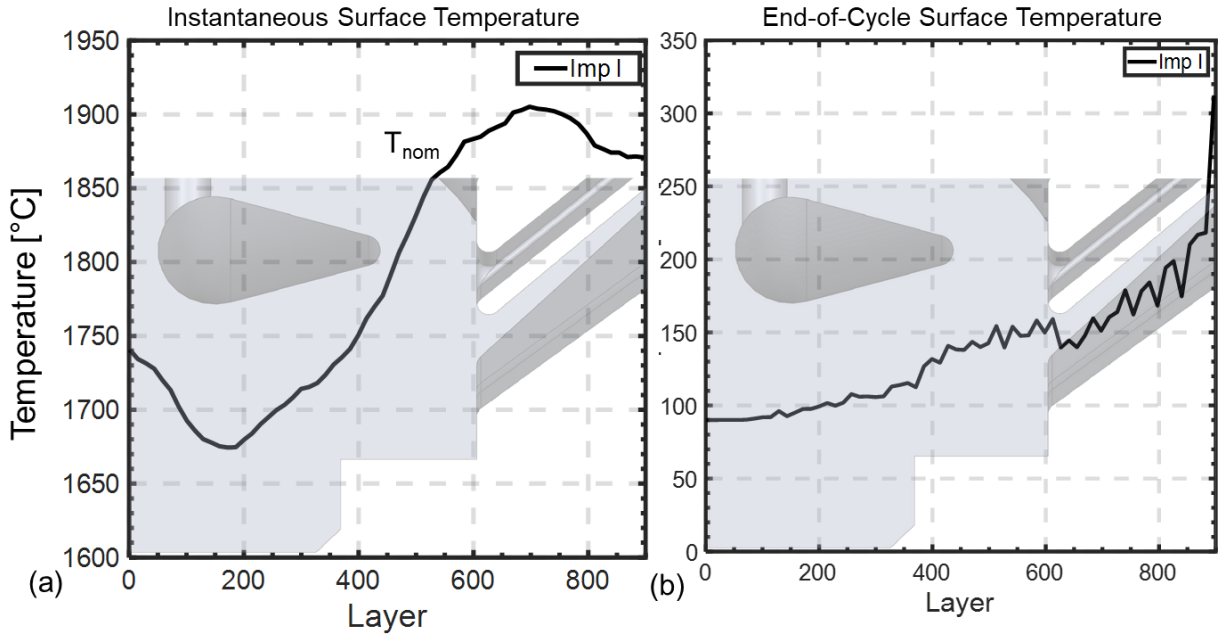

Figure 15: Thermal history for the entire part (a) sampled at 0.1 seconds after the laser strikes the part, and (b) at the end-of-cycle temperature. The instantaneous surface temperature in (a) is evocative of the short-time process dynamics dominated by the laser-meltpool interactions, and exceeds the melting temperature of the material . The end-of-cycle temperature trends in (b) are influenced by the geometry of the part. In both cases the temperature increases with the build height, owing to the decrease in the time between layers, and reduced cross-section.

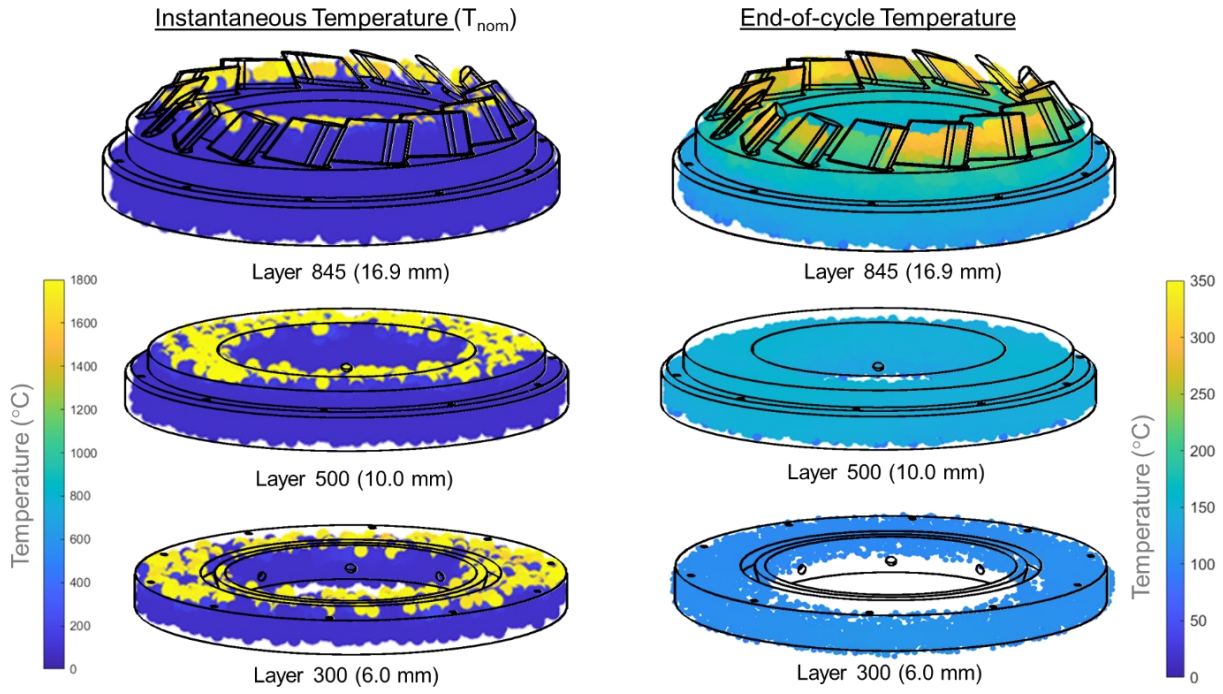

Figure 16: Comparison of the simulation result when using the instantaneous temperature (left) and the end-of-cycle temperature (right). The end-of-cycle temperature distribution is lower because the laser-added heat has time to diffuse throughout the part .

2.3.2 *Phase II (Monitoring Phase) – Qualify-as-you-build*

The aim of Phase II is to detect flaw formation when building a new part of the same shape, i.e., monitor part quality of another impeller as it is being printed. For this purpose, Phase II uses the thermal history (T_{nom}) of the nominal flaw-free part obtained offline in Phase I in Eqn. (12). Consequently, the thermal model predictions from Phase I are not static and are updated in layer-by-layer based on streaming sensor data to detect flaw formation. As the following will show, the monitoring step does not require re-computation of the thermal history using the graph theory approach and is nearly instantaneous.

The interlinking of Phase I – mirror-as-you-build, and Phase II – qualify-as-you-build is represented schematically in Figure 17. It conceptually depicts the methodology of updating the already existing thermal history predictions ($T_{nom}(l)$) for Impeller I obtained in Phase I contingent on the meltpool temperature at layer l for the new part, $TEP_{new}(l)$. The rationale is that the thermal history of a new part, $T_{new}(l)$ (for Impeller II, III, and IV), is liable to contain both the common cause variation inherent in the process (viz., captured in the thermal history of Impeller I) and the special cause variation resulting from flaws.

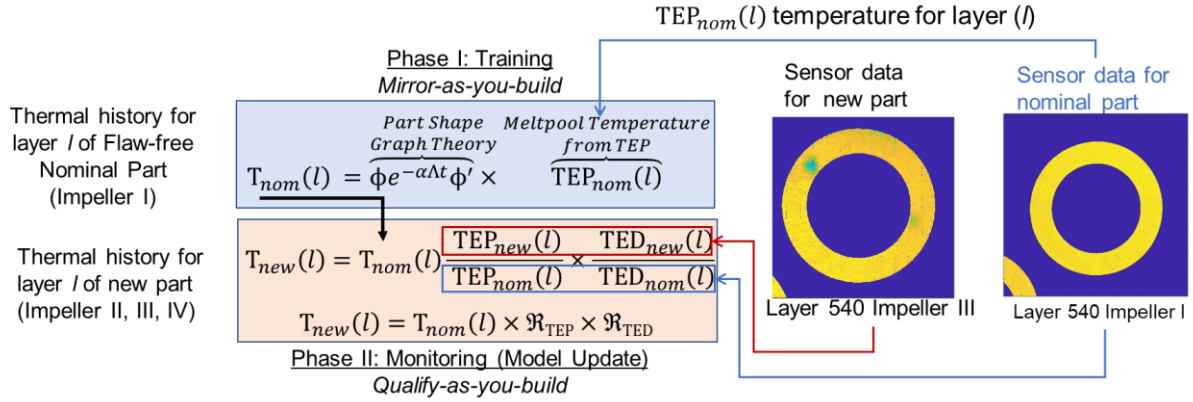

Figure 17: The two phases of the digital twin approach for detecting flaw formation. In Phase I, mirror-as-you-build, a baseline thermal history for a nominal flaw-free part is established (T_{nom}). In Phase II, qualify-as-you-build, the thermal history of a new part T_{new} is obtained by instantaneously updating the thermal history of the nominal-flaw free part T_{now} and the streaming data for the new part.

The approach to update the thermal history for a new part is as follows. At the outset we write the temperature T_{new} at the sampled location at layer l using the same reasoning in Phase I, Eqn. (12).

$$\mathrm{T}_{new}(l) = \mathbb{S}(l) \times \mathrm{TEP}_{new}(l) \tag{14}$$

The term $\mathbb{S}$ is obtained from Eqn. (12) from Phase I, as $\mathbb{S}(l) = \frac{\mathrm{T}_{nom}(l)}{\mathrm{TEP}_{nom}(l)}$

Substituting the foregoing for $\mathbb{S}$ into Eq. (14),

$$\mathrm{T}_{new}(l) = \mathrm{T}_{nom}(l) \times \frac{\mathrm{TEP}_{new}(l)}{\mathrm{TEP}_{nom}(l)} \tag{15}$$

The above equation is simplified on writing $\mathfrak{R}_{\mathrm{TEP}(l)} = \frac{\mathrm{TEP}_{new}(l)}{\mathrm{TEP}_{nom}(l)}$

$$\mathrm{T}_{new}(l) = \mathrm{T}_{nom}(l) \times \mathfrak{R}_{\mathrm{TEP}(l)} \tag{16}$$

In other words, the thermal history of a new part at layer l, $\mathrm{T}_{new}(l)$, is obtained by updating the thermal history of the nominal part $\mathrm{T}_{nom}(l)$, and relative change $\mathfrak{R}_{\mathrm{TEP}(l)}$ in the in-process meltpool temperature of the new part $\mathrm{TEP}_{new}(l)$ at layer l with respect to the nominal part $\mathrm{TEP}_{nom}(l)$.

Next, we incorporate the effect of changes in the laser power (energy density) relative to the nominal impeller, through the TED sensor measurements as follows,

$$\mathrm{T}_{new}(l) = \mathrm{T}_{nom}(l) \times \mathfrak{R}_{\mathrm{TEP}} \times \frac{\mathrm{TED}_{new}(l)}{\mathrm{TED}_{nom}(l)} = \mathrm{T}_{nom}(l) \times \mathfrak{R}_{\mathrm{TEP}} \times \mathfrak{R}_{\mathrm{TED}} \tag{17}$$

It is necessary to incorporate both the TEP and TED data to update the thermal history as these provide complementary information. As will be evident in Sec. 3.2, the TEP captures the interaction of the laser and powder; it is sensitive to the effect of part shape on the thermal history. Whereas TED captures variation between parts resulting from change in the global energy density. While the *theoretical* global energy density (Ev) can be estimated as a function of the laser power (P), velocity (v), hatch spacing (h), and layer thickness (d), $\mathrm{Ev} = \mathrm{P}\cdot\mathrm{v}^{-1}\cdot\mathrm{h}^{-1}\cdot\mathrm{d}^{-1}$ the measurements captured by the TED sensor are capture the actual energy density applied to a layer. Moreover, the TED data is readily integrated into the graph theory thermal model since it is unitless.

Since, the thermal history of the nominal part $T_{nom}(l)$ has been obtained in Phase I, the computation time in obtaining $T_{new}(l)$ is infinitesimal and can be completed before the next, (l +1) layer is deposited. The initial computational effort is expended to obtain in $T_{nom}(l)$ in Phase I, which is an offline phase. As detailed in the next section Sec. 2.3.3, Phase I requires 7 minutes to converge on a desktop computer compared to 16.5 hours of actual build time. Finally, flaw formation in new parts is detected by comparing the thermal history of the new part $T_{new}(l)$ with the thermal history of the nominal part $T_{nom}(l)$. For example, a large deviation in the thermal history of a new impeller from the nominal impeller at layer *l,* i.e., $T_{nom}(l) - T_{new}(l)$, would be indicative of an incipient flaw.

2.3.3 Model Parameters, Calibration and Convergence

The graph theory approach requires the calibration of three model parameters, referring to Eq. (2), these are: the number of nodes in terms of their density n [nodes·mm^{-3}]; the number of super layers (meta layers, SLT, [mm]) that are considered to be deposited at the same time for computational efficiency; and the gain factor g. In this work, the gain factor is identical to our previous work in which the graph theory approach was applied to 316L stainless steel parts [44, 48]. The model parameters are detailed in Table 2.

Shown in Figure 18(a) and (b) are the convergence characteristics of the graph theory model as a function of the node density and superlayer thickness, respectively. Increasing the node density and reducing the superlayer thickness improves the prediction accuracy at the cost of computational efficiency. The effect of the node density and super layer thickness on the computational time is reported in Table 3. For example, in Figure 18(b) the convergence of the

model is tested for SLT ranging from 1 mm to 0.15 mm. An appreciable degree of convergence is observed for SLT = 0.25 mm.

In this work, as reported in Table 3, the trends converge within 7 minutes with number of nodes set at 0.5 nodes·mm^{-3}, and superlayer thickness of SLT =0.25 mm (12.5 actual layers, each of 0.020 mm). At finer SLT = 0.20 mm and 0.15 mm, the computation time increases significantly to 11 minutes and 13 minutes, respectively, for a marginal difference in convergence characteristics. Thus, as a tradeoff between computation and model resolution, we set n = 0.5 nodes·mm^{-3} and SLT = 0.25 mm. The thermal history predicted from adopting these parameters are shown in Figure 19 overlaid on the normalized TEP signatures observed for Impeller I (the TEP data from Figure 11 are smoothened to match an SLT = 0.25 mm). With SLT = 0.25 mm and node density n = 0.5 nodes·mm^{-3}, the graph theory approach accurately predicted the drop in temperature in the layers corresponding to the internal channel, as well as towards the end of the fin region observed in the TEP data.

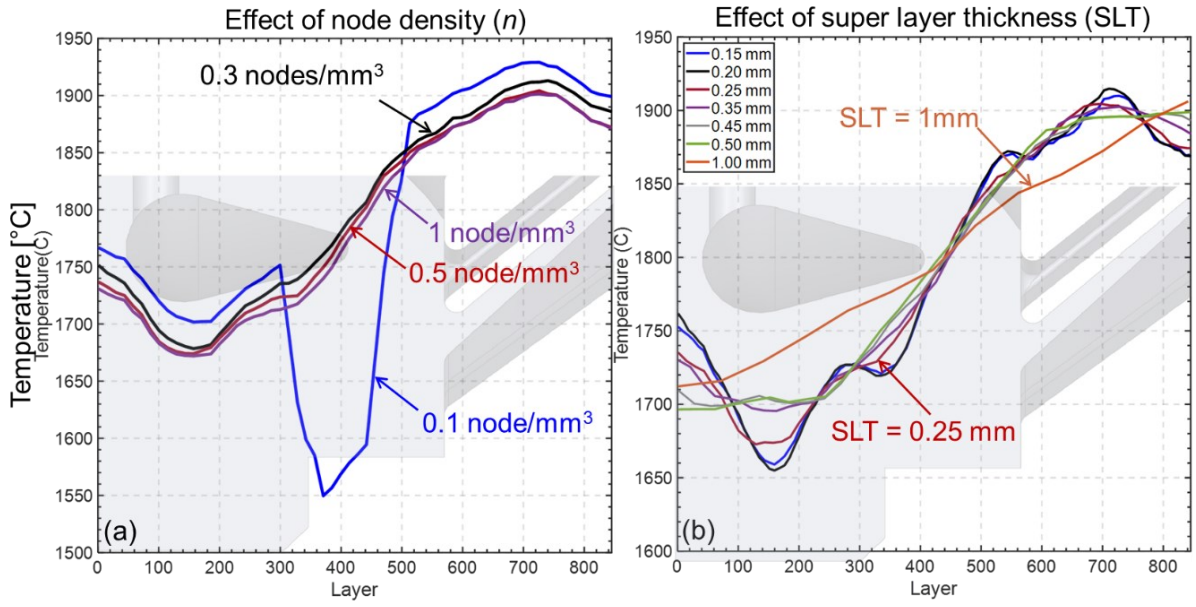

Figure 18: The convergence studies with (a) effect of the node density (n) with super layer thickness (SLT) fixed at 0.25 mm, and (b)effect of SLT with node density fixed at n = 0.5 nodes·m^{-3}. In this work we set n = 0.5 nodes·m^{-3} and SLT = 0.25 mm.

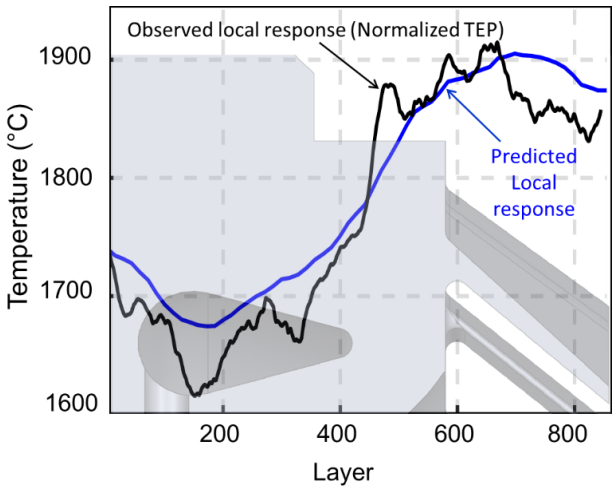

Figure 19: With super layer thickness (SLT) fixed at 0.25 mm, and node density n = 0.5 nodes^{-3}, the local response predicted from the graph theory approach closely matches the observed TEP (normalized) trends.

As a qualitative comparison, the graph theory approach was corroborated with the commercial Netfabb software assuming identical super layer thickness, and laser power and velocity. As evident from Figure 20, both the graph theory and Netfabb predict the retention of heat in the fin region of the impeller. The graph theory predictions shown in Figure 20 were obtained by assuming a steady-state end-of-cycle melting temperature T_0 of ~1370 °C (approximate melting point of SAE 316L), instead of the instantaneous meltpool temperature T_{nom} used for flaw monitoring. This is because Netfabb, and other commercial LPBF software, do not facilitate incorporation of the instantaneous meltpool temperature.

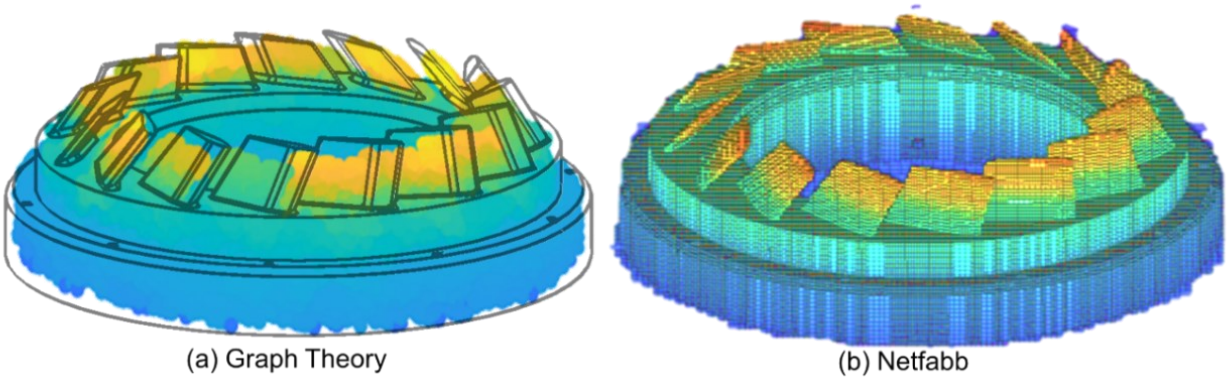

Figure 20: The graph theory-derived steady state thermal history predictions compared with the commercial Netfabb output.

Table 2: The material properties and simulation parameters used in this work.

Material Properties	**Values**
Convection coefficient part to powder, hw [W·m^{-2}· C]	1×10^{-5}
Convection coefficient substrate (sink), hs [W·m^{-2}· C]	1.0×10^{-2}
Thermal diffusivity (α) [m^2/s]	3.0×10^{-6}
Density, ρ [kg/m^3]	8,190
Steady state melting point (T_0) [°C]	1,370
Ambient chamber temperature, T_p [C]	90
Simulation Parameters	Values
Characteristic length [mm]	2
Fixed number of nearest neighbors (η)	10
Superlayer thickness (SLT) [mm]	0.25 (12 actual layers)
Node density, (*n*) [nodes·m^{-3}]	0.5
Gain factor (g) [m^{-2}]	2×10^5 from Ref. [44, 48]
Computational hardware	Intel Core i7-6700 CPU, @3.40 GHz with 32 GB RAM.

Table 3: The effect of node density superlayer thickness on computation time. In this work we selected a node density of 0.5 nodes·mm^{-3} and a 0.25 super layer thickness.

Node Density [nodes·mm^{-3}]	Super Layer [mm]	Total number of Nodes	Simulation Time [s]
0.1	0.25 (selected, 12.5 layers)	1407	23
0.3		4083	121
0.5 (selected)		6771	393
1		13748	2393
0. 5	0.15	6771	796
	0.20		675
	0.25 (12.5 layers)		393
	0.35		277
	0.45		181
	0.5		179

3 Results

3.1 Post-Process Characterization

3.1.1 X-ray Computed Tomography

The four impellers were examined using XCT (NorthStar Imaging, NSI) at voxel resolution of 26 µm. Shown in Figure 21 are the XCT section views for the four impellers. The corresponding flaw volume as a percentage of the total volume are reported in Table 4. These flaws were of the lack-of-fusion type given their characteristic irregular shape, evident in the forthcoming Sec. 3.1.2. Lack-of-fusion flaws are caused when the energy density is insufficient to entirely consolidate the powder.

Impeller I (Nominal), which was processed with a laser power fixed at 195 W had the least percentage flaw volume (0.01%). For the rest of the parts the percentage flaw volume ranges from 0.08% to 0.11%. The flaws in Impeller II were predominantly clustered near the fin region, corresponding to the transition in the laser power from 195 W to 125 W. The clustering of flaws at a particular location was also observed in Impeller III. The clustering of flaws in Impeller III was due to lens delamination. Lens delamination causes laser focus aberrations, leading to insufficient fusion. In contrast, for Impeller IV, the lack-of-fusion flaws were evenly distributed throughout the part, as it was processed entirely at low-level of laser power of 125 W.

Table 4: The flaw characteristics for each of the four impellers, including the flaw volume ratio.

Impeller	Flaw Volume [mm^3]	Total Part Volume [mm^3]	Flaw Volume Ratio [%]
Impeller I (Nominal Conditions)	1.29	18497	~ 0.01
Impeller II (Nominal-Lo)	19.10		~ 0.11
Impeller III (Nominal-Hi) + Lens Delamination	15.23		~ 0.09
Impeller IV (Lo-Lo)	13.29		~ 0.08

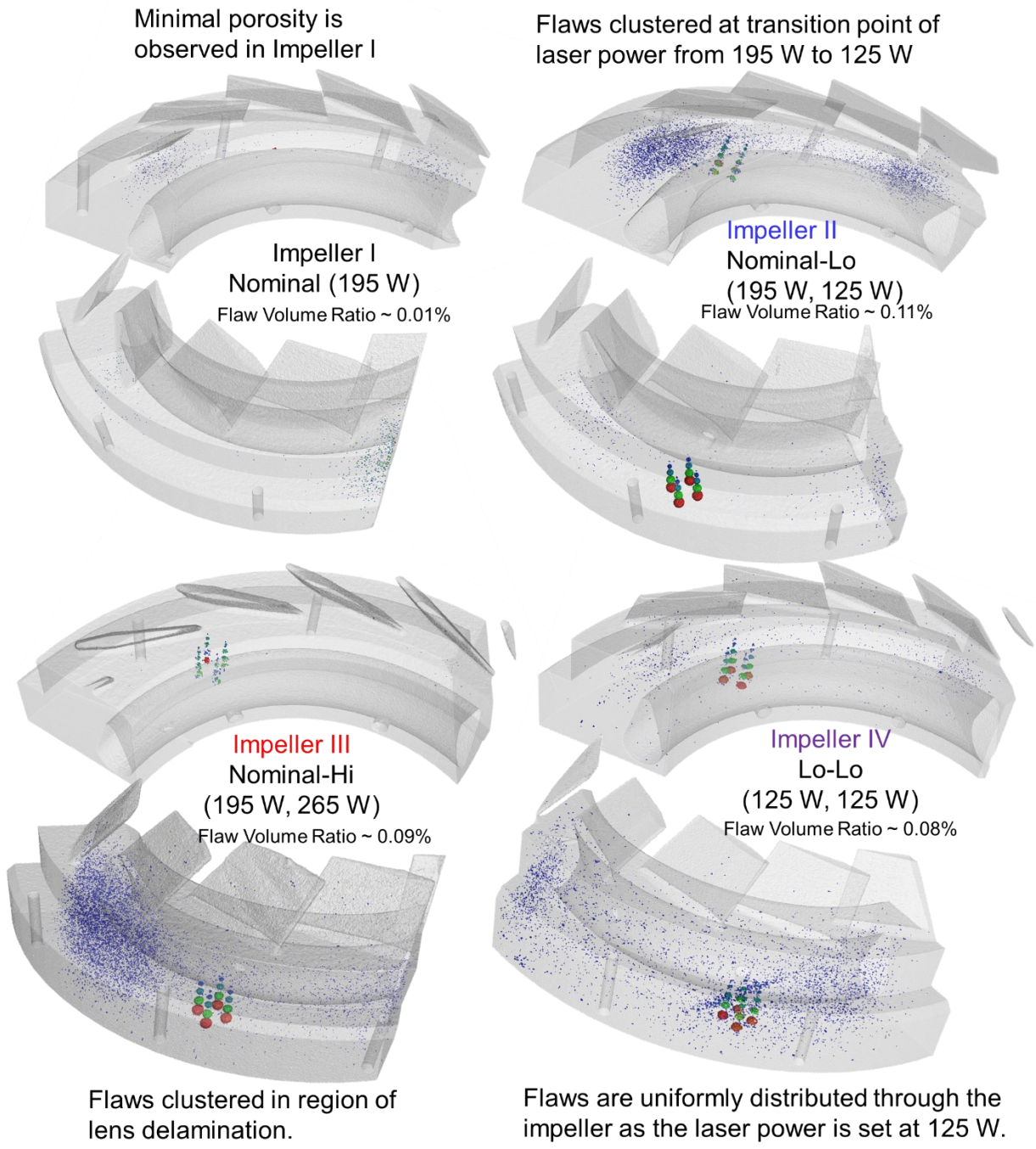

Figure 21: X-ray computed tomography (XCT) images of the two quarter-sections of each of the four impellers. Impeller I produced under nominal conditions has few pores (~ 0.01%), compared to Impellers II, III, and IV. In Impeller II the flaws tend to occur in the region between the mid and fin-section at the transition point when the laser power is reduced from 195 W to 125 W. In Impeller III flaws are clustered in the region of lens delamination. Impeller IV is produced at 125 W which results in lack-of-fusion porosity throughout the part.

3.1.2 Optical Microscopy

The optical micrographs for cross-sections of the four impellers after polishing and etching using Kalling's #2 reagent are shown in Figure 22. Three regions of each impeller: base (A), mid (B), and fin (C) were examined. Lack-of-fusion flaws, characterized by their irregular shape, and ranging between 30 μm to 100 μm in size are observed in the optical micrographs.

Affirming the XCT analysis from Sec. 3.1.1, Impeller I produced under nominal conditions (195 W laser power, 100 $J \cdot mm^{-3}$) did not depict extensive lack-of-fusion flaw formation. Lack-of-fusion flaws were prominent in Impeller II (nominal-Lo), and Impeller IV (Lo-Lo). The reduction in laser power from 195 W to 125 W during processing of the fin section of Impeller II is the likely cause of these lack-of-fusion flaws as the energy is insufficient for complete consolidation of the material. In a similar vein, the processing of Impeller IV at a reduced laser power of 125 W results in considerable lack-of-fusion.

The fin section of Impeller III, which was produced under Nominal-Hi conditions, has a distinctively coarser microstructure compared to its base and mid regions (of Impeller III). Moreover, the grain size in the fin region of Impeller III was significantly coarser relative to the fin regions of other parts. Such grain coarsening is liable to occur on account of heat accumulation and is further quantified in Sec. 3.1.3 [22].

To explain further, the fin region has the smallest cross-section and the least time between layers (TBL). As noted from Figure 5, for the base and mid sections the TBL is nearly 120 seconds and 80 seconds, respectively, compared to approximately 20 seconds in the fin region. The increase in laser power from 195 W to 265 W, reduction in cross-section, and decrease in the TBL combine to exacerbate the heat accumulation in the fin region. The heat accumulation in the fin region,

which was predicted by the graph theory simulation in the context of Figure 15 and Figure 16, explains the coarsening of the grains in the fin section of Impeller III observed in Figure 22.

In closing this section, we note the possibility of keyhole flaw formation, particularly in the fin region of Impeller III when laser power was increased to 265 W. However, keyhole flaw formation was not captured either in the XCT (Figure 21) nor in the optical images (Figure 22). This is because, keyhole porosity is typically smaller than 30 μm [5]. Since, the resolution of the XCT in this work is 26 μm, its ability to detect keyhole porosity is rather limited. The optical images are produced for one contiguous cross-section of the impeller, given their rarity and small size, the presence of keyhole porosity was not captured in the optical microscopy images.

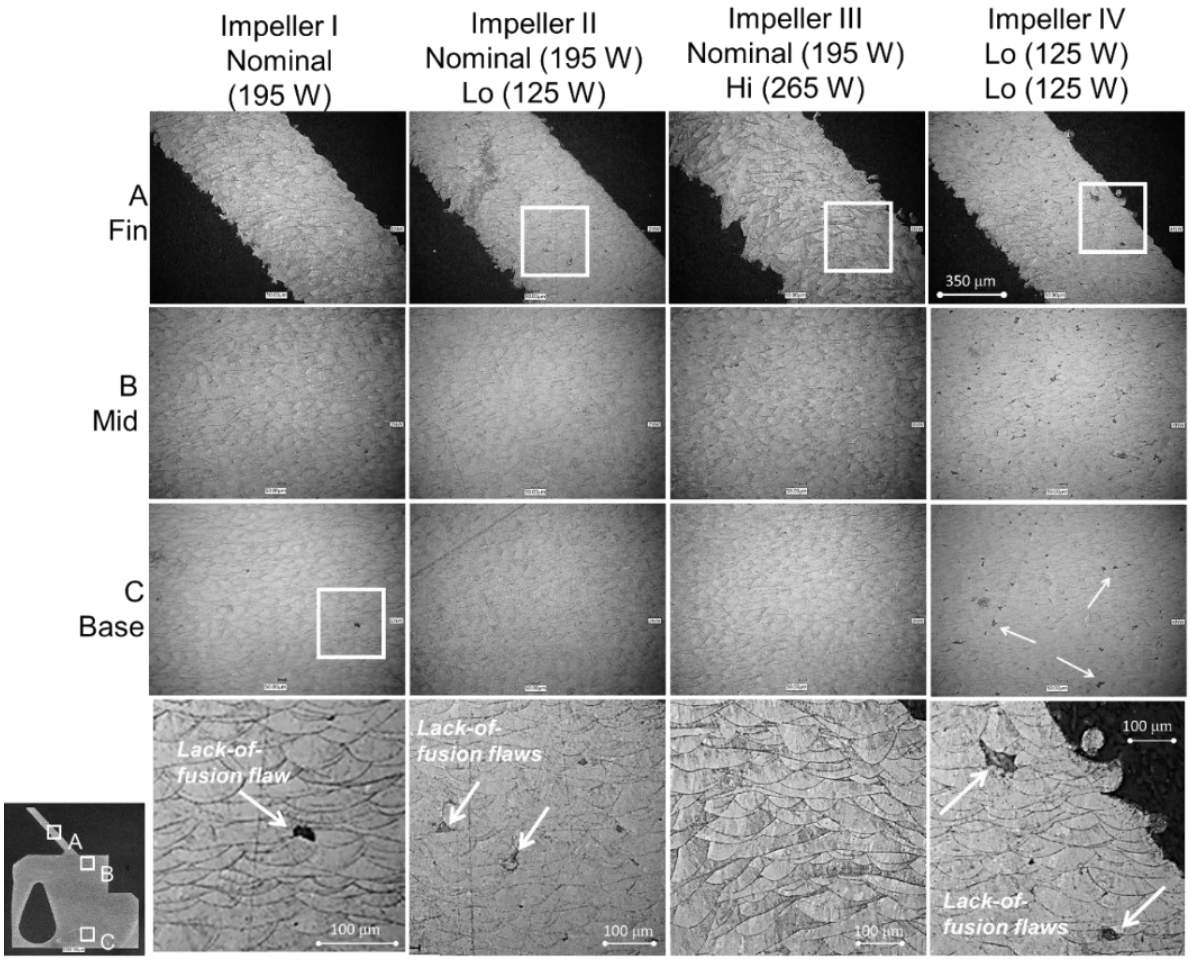

Figure 22: Effect of change in processing conditions on the microstructure and porosity. Optical microscopy images are acquired at three regions of each impeller, corresponding to (A) fin, (B)

mid, and (C) base sections. The bottom-most row of images are zoomed-in views of the demarcated regions for each impeller. There are notably large number of pores in the fin-section for Impeller II which was produced under the Nominal-Lo condition (195 W – 125 W). The fin-region of Impeller III, produced under Nominal-Hi (195 W – 265 W) conditions has coarser microstructure compared to others. Impeller IV, which is produced under low power settings of 125 W shows presence of lack-of-fusion porosity along its entire cross-section.

3.1.3 Scanning Electron Microscopy (SEM) and Electron Backscatter Diffraction (EBSD)

Each of the four impellers was cross-sectioned along the build direction using electro-discharge machining, and were prepared by ground, polished, and etched (Adler's reagent). Subsequently, the samples were examined with SEM and EBSD (FEI Quanta 600-ESEM) to understand and quantify the variation in grain size, crystallographic orientation (texture), and porosity. The SEM and EBSD results are reported in Figure 23 and Table 5. The samples were measured at 15 kV, working distance of 21.2 mm, spot size of 5 μm, and scanning step size 1 μm.

In Figure 23, Impeller I, viz., made under nominal laser power parameters (195 W) manifests variations in the grain size between the fin and base. This is consistent with prior explanations in the context of the XCT (Figure 21) and optical micrographs (Figure 22) due to the differences in the cross-section of the and the time between layers. The average grain size is larger in the fin section of Impeller I compared to the base section due to heat retention in the fin region as predicted in the simulation (Figure 15) and observed in the data (Figure 11). The SEM results in Figure 23 also reveal lack-of-fusion formation in Impeller I, albeit sparse, as highlighted with the yellow circles.

The grain sizes in Impeller II fin region are smaller than that of the base region, as observed in Table 5. This is because the laser power is decreased to 125 W from 195 W in the processing of the fin region. It is further seen that <111> (note that all measurements reported herewith are along the build direction) columnar grains in the base region have a tendency of forming <101> grains as layers were added due to the low laser power. This likely because the activation energy

necessary for reorientation and grain growth was not reached, and the distribution of small equiaxial grains was increased. For Impeller III, the use of higher laser power in the fin region, in combination with reduced time between layers and cross-section area leads to heat accumulation, which explains the large increase in grain size observed in Table 5 consistent with literature, and prior observation with the optical micrography shown in Figure 22 [26, 44, 68].

Moreover, the base regions of Impellers I, II, and III show prominent chevron-like solidification structures [69]. Additionally, processing the fin region of Impeller III at high laser power of 265W induced crystal growth along with the z (build) direction and a higher crystallographic misorientation angle >15˚. Furthermore, the fin region of Impeller III shows more <101> columnar grains than its base region. The base region was found to be composed of <111> columnar grains with stronger epitaxy in <001>. Several randomly oriented smaller grains may have also occurred by the nucleation of new grains in the fin region. Also evident in the fin region of Impeller III are circular-shaped flaws of approximate size 30 μm

In contrast, the fin region of Impeller IV showed dominant columnar grain growth along the <111> direction compared with the base region which has grains in the <101> with the additional presence of <001> grains. As described in recent findings by Oliveira *et al.* [70], these observation as explained as a result of preferential growth direction during solidification in additive manufacturing.

In closing this section, from the grain size metrics shown in Table 5, it is deduced that the grain size is larger under high power conditions and typically reduces as the power decreases. The larger mean and standard deviation in grain size observed in the fin region in comparison to the base region for Impeller I, III and IV suggests that not only the change in power but also the change in time between layers and cross-section area.

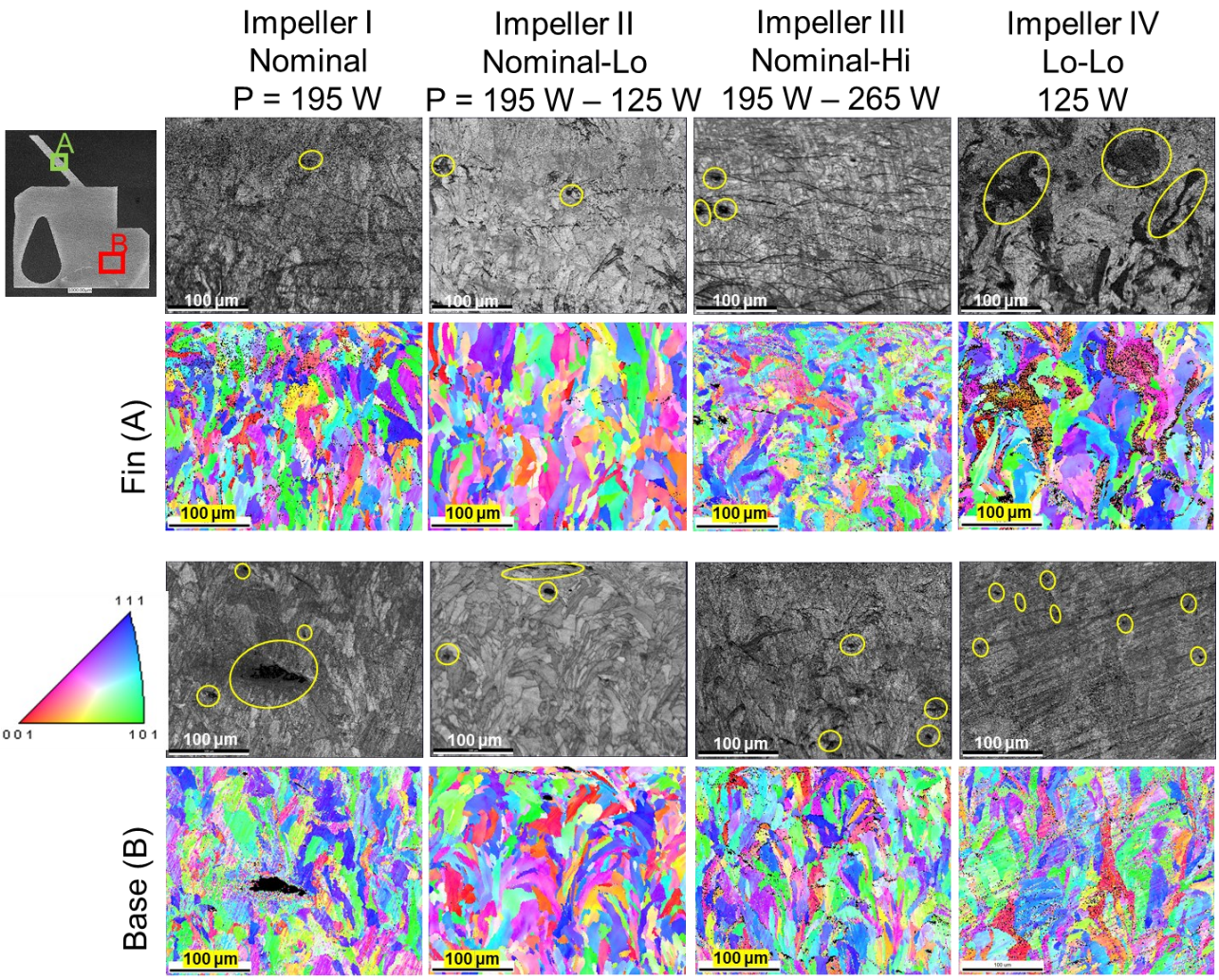

Figure 23: SEM images and inverse pole figure (IPF) EBSD images with respect to z (build direction) showing the effect of laser power on the grain size and orientation for all impellers-fin (A) and base (B) regions. The yellow circles demarcate lack-of-fusion flaws.

Table 5: Grain size analysis for fin and base regions of all impellers. Over 200 grains were measured for obtaining the mean and standard deviation.

		Impeller I Nominal	Impeller II Nominal-Lo	Impeller III Nominal-Hi	Impeller IV Lo-Lo
Base (B)	Average Grain Size (µm)	16.0	16.6	21.2	16.3
	Standard Deviation (µm)	12.11	8.28	11.30	10.62
Fin (A)	Average Grain Size (µm)	20.6	14.0	21.5	17.8
	Standard Deviation (µm)	13.74	7.79	11.53	10.20

3.2 Process Signatures

3.2.1 Case I - Effect of change in process parameters (process drifts)

The TEP measurements sampled at locations without planted flaws for the four impellers are shown in Figure 24 as a function of the layer height. As evident from Figure 24(a) and (b) all impellers exhibited similar TEP responses, with an increase in the fin region, indicating the consequential effect of part shape (geometry) in influencing its thermal history.

In Figure 24 (b), the TEP measurements for Impeller IV are smaller in comparison to Impeller II and III as it was produced entirely at the low-level laser power of 125 W. However, in Figure 24(b) the TEP measurements are not significantly different between Impeller II and Impeller III despite the change in laser power in the fin-region. As noted previously in Sec. 2.1.2, in the fin region of Impeller II the laser power was decreased from 195 W to 125 W; the laser power in the fin region for Impeller III was increased from 195 W to 265 W. Further, the TEP signature for Impeller II, did not reduce in the fin region to the same level as Impeller IV even though the laser power was reduced to 125 W.

The TED measurements sampled at locations without planted flaws are shown in Figure 25. Unlike TEP measurements, the TED measurements varied prominently between the sections of the impeller produced under differing laser power conditions. This is because the TED measurements were obtained from broadband build chamber emissions symptomatic of variation in the global energy density (E_v). However, the TED measurements do not capture variation in the thermal history resulting from the part geometry, and as will be evident shortly in Sec. 3.2.3, nor is TED sensitive to f-θ lens delamination flaws (Case III). In other words, the TEP and TED data are complementary, TEP is more sensitive to the variations in the thermal history on account of the change in part shape and lens transmission flaws whereas, TED captures variation in the thermal history resulting from change in the global energy density.

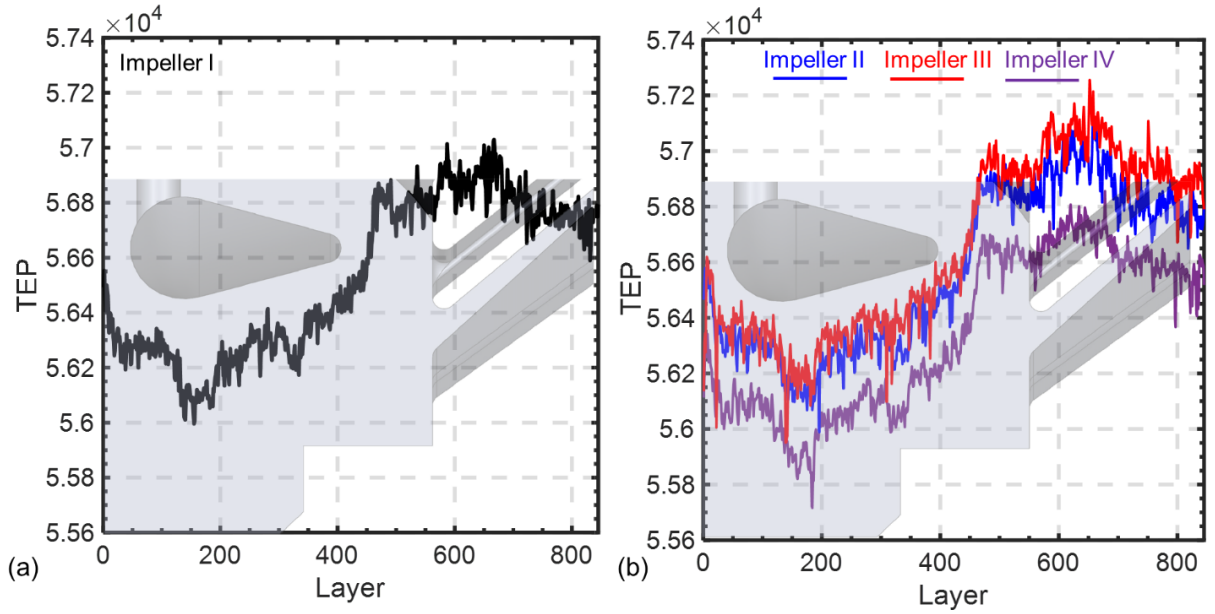

Figure 24: (a) TEP signatures for Impeller I (nominal). (b) TEP data for Impeller II, III and IV. Except Impeller IV, which is consistently produced at low power of 125 W for all sections, there is no significant difference in the TEP measurements. We also note that the TEP measurements increase with the build height and reach a peak value for all sensors in the region of the fin due to its reduced cross section.

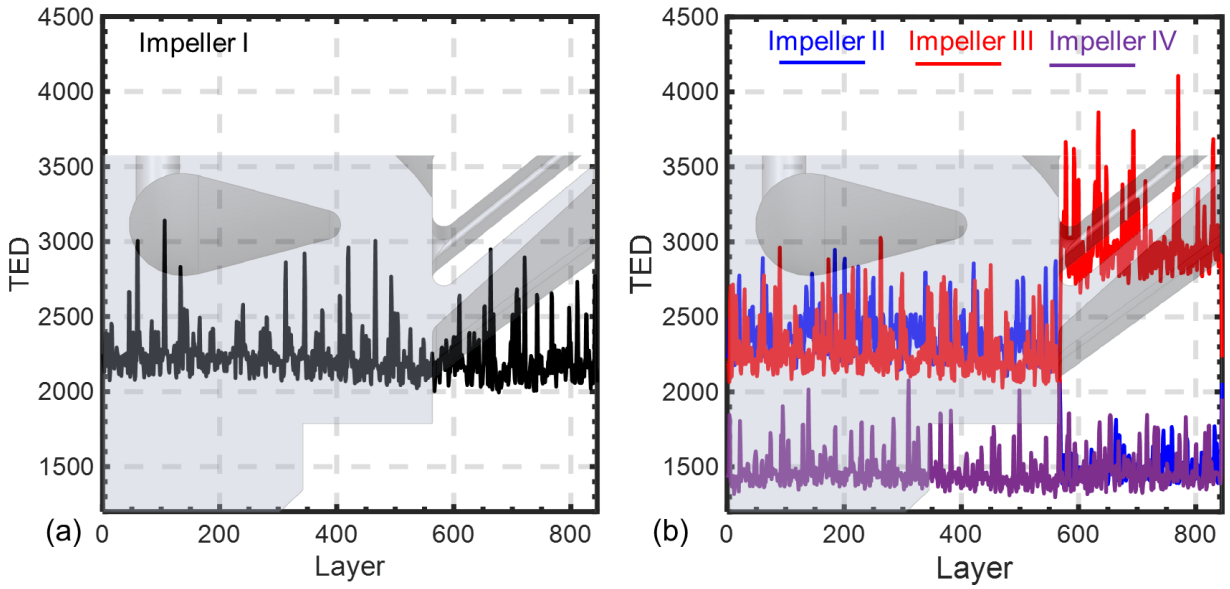

Figure 25: (a) TED photodetector response for each Impeller I produced under nominal conditions. (b) TED measurements for Impellers II, III, and IV capture the deviations from the nominal laser.

3.2.2 Case II – Effect of Planted Flaws

Figure 26 (a) and (b), respectively, show the TEP and TED signatures averaged over a layer at locations where flaws (voids) were deliberately planted. In both measurements large deviations (spikes) were observed at locations with embedded flaws due to partially fused and unmelted powder trapped inside the voids. Six such spikes are evident in Figure 26, corresponding to the six largest diameter flaws – Φ 0.5 mm, Φ 0.4 mm, Φ 0.3 mm, Φ 0.2 mm, Φ 0.1 mm, and Φ 0.05 mm. The smallest planted flaws of Φ 0.03 mm were not readily discerned in the sensor measurements. The sensor measurements are therefore sensitive to flaw sizes larger than Φ 0.05 mm.

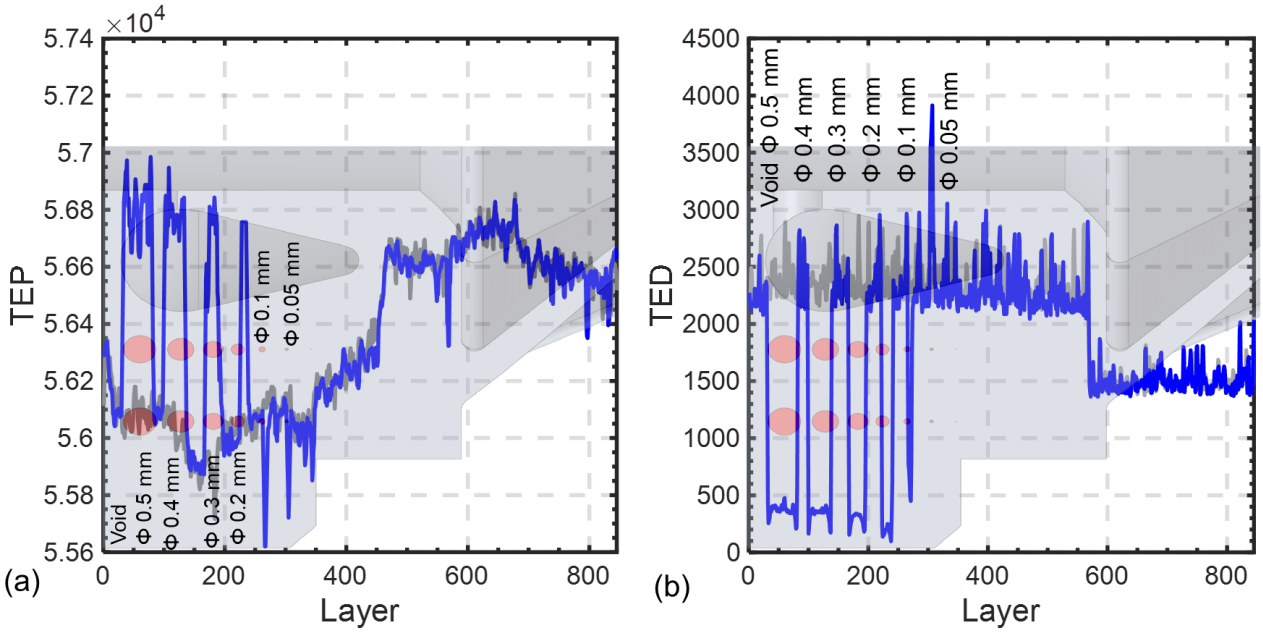

Figure 26: Effect of planted flaws on (a) TEP and (b) TED measurements relative to trends for a flaw-free region (grey line). The spikes in the TEP and TED correspond to the presence of flaws. Flaws as large as 0.050 mm (50 µm) are discerned from the signal characteristics.

3.2.3 Case III – Effect of Lens Delamination

The representative TEP measurements for the region of Impeller III afflicted with lens delamination are shown in Figure 27. The TEP and TED trends over a 3 pixel × 3 pixel region are plotted in Figure 28 (a) and (b) respectively. The effect of lens delamination is evident in the relative low intensity of the TEP signature in Figure 28 (a). These regions of lens delamination appear consistently over multiple layers of the base and mid-section until only a small area persists in the fin region.

The effect of delamination is evident when comparing the TEP signatures of Impeller III for a region with lens delamination and a region without lens delamination region. Such a comparison of TEP signatures is depicted in Figure 28 (a). This difference in intensity of the TEP signature persists until the fin region. The increase in laser power from 195 W in the base and mid-section to 265 W in the fin region during the processing of the fin region of Impeller III, coupled with its smaller surface area negates the deleterious impact of lens delamination.

In contrast to the TEP signatures, the TED signature in Figure 28 (b) did not register any discernable difference when sampled between the regions with and without lens delamination. This limitation is explained by Mani *et al.* [9]. For capturing optical transmission effects using co-axial monitoring systems, Mani *et al.* note that it is necessary to measure the process radiation in a narrow frequency region close to the bandwidth of the f-θ lens to eliminate noise from the chamber radiation. The TEP signature is a filtered measurement, whereas TED provides an unfiltered broadband measurement. Hence it is to be expected that the TED measurement did not register the onset of lens delamination.

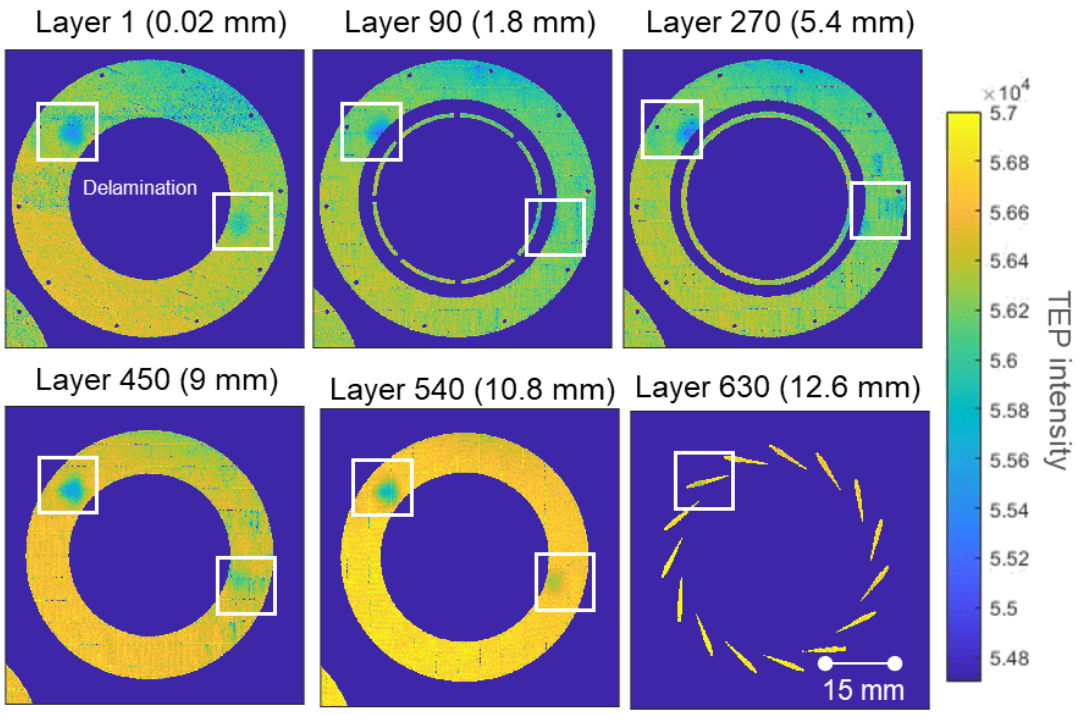

Figure 27: Representative layer-wise TEP measurements for six layers of Impeller III. In the demarcated locations, these TEP measurements show the presence of regions affected by lens delamination. Note the areas of persistent low intensity in the northwest quadrant.

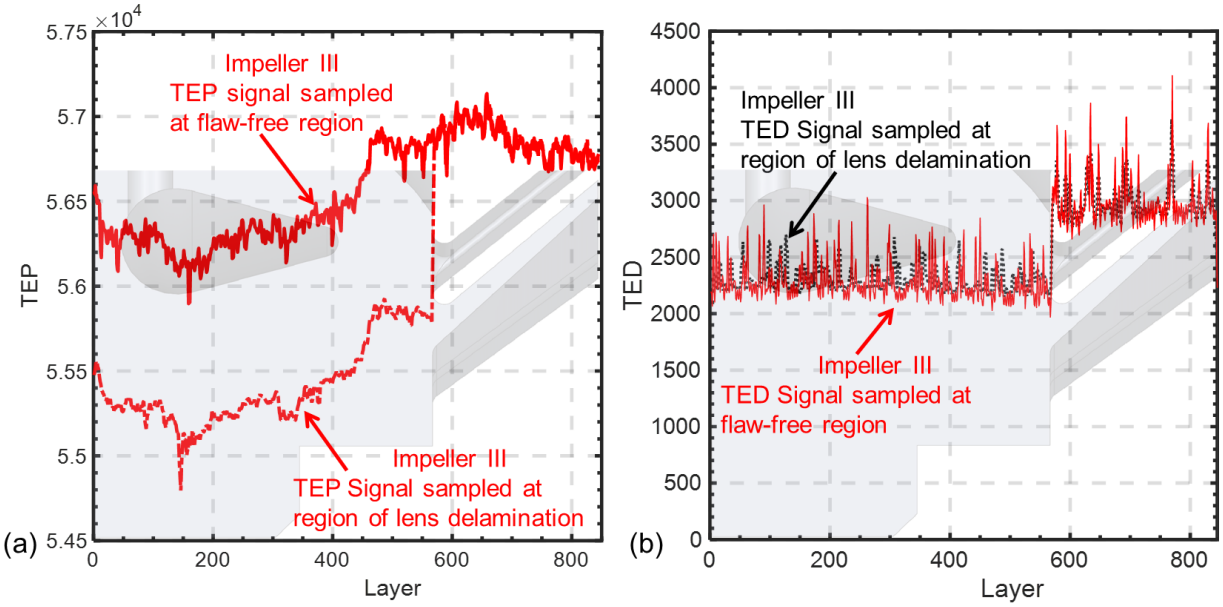

Figure 28: Comparing (a) TEP and (b)TED measurements sampled at flaw-free regions (solid line) and at regions with lens delamination (dotted line). (a) There is a significant difference in the TEP trends prior to the melting of the fin region corresponding to the location of lens delamination. (b) The TED signatures for flaw-free and delamination-afflicted regions are visually undistinguishable.

Figure 24 through Figure 28 thus reveal the effectiveness and complementary nature of the TEP and TED measurements in capturing potential flaws resulting from both process drifts and planted flaws. However, the following limitations and challenges impede the direct use of the TEP and TED sensor measurements for flaw monitoring.

- The TEP and TED data were acquired at a sampling rate of 200 kHZ and 100 kHZ, respectively, and continuously throughout the 16.5-hour build (845 layers). Data amounting to 3 gigabytes of two types of process signatures (TEP and TED) were obtained in this work. Therefore, to detect flaw formation the sensor signatures the data must be transferred for further analysis. The inherent latency in the transfer and analysis of the large volume of sensor signatures prevents prompt detection of flaws.
- The process signatures contain information from both common cause variations resulting from the part shape, as well as special cause variations from change in laser power (Case I, Figure 24 and Figure 25), embedded voids (Case II, Figure 26), and lens delamination (Case III, Figure 27). For example, in Figure 24 the TEP signatures increase during the processing of the fin region even when the processing conditions are held constant (Impeller I and IV). In the absence of a physics-based model to delineate the thermal trends, it is challenging to separate such naturally occurring variations (common cause variation resulting from the part shape, location, orientation, scanning pattern) from variations in the sensor signatures caused by incipient flaws (special cause variation, such as machine faults, cyber intrusion, change in process parameters, recoater crash).

3.3 Application and Results of the Digital Twin Approach

3.3.1 Case I – Detecting change in process parameters (Process Drifts)

As described in Eqn. (17), the meltpool information in the form of TEP and TED signatures was incorporated into the graph theory thermal model. Figure 29(a) shows the instantaneous surface temperature predictions for the four impellers as a function of layer height. The instantaneous surface temperature (T_{nom}) being the local response following 0.1 sec after the laser strikes the sampled area as described in the context of Figure 14 and Figure 15 from Sec. 2.3.2.

Figure 29(b) shows the surface temperature predictions at the end-of-cycle. Comparing Figure 29(a) and (b) underscores the importance of considering the instantaneous surface temperature as opposed to the end-of-cycle temperature. The end-of-cycle temperature trends shown in Figure 29(b) fail to capture and identify process drifts resulting from changes in the laser power.

The instantaneous surface temperature Figure 29(a) diverges significantly for Impellers II, III, and IV, corresponding to the layers where the laser power is changed. A comparison of Figure 29(a) and Figure 24 highlights the utility of the digital twin approach – process anomalies that are difficult to discern from the TEP sensor data alone are revealed prominently when the sensor signatures are combined with a physical model. Moreover, the data need not be subjected to further analysis.

The deviation in thermal trends of Impeller II, III, and IV compared to the thermal trends of the nominal Impeller I are charted in Figure 30, i.e., Tnew - Tnom. The deviation in thermal history for Impellers II and III is significant in the fin region where the laser power was changed from 195 W to 125 W and 265 W , respectively.

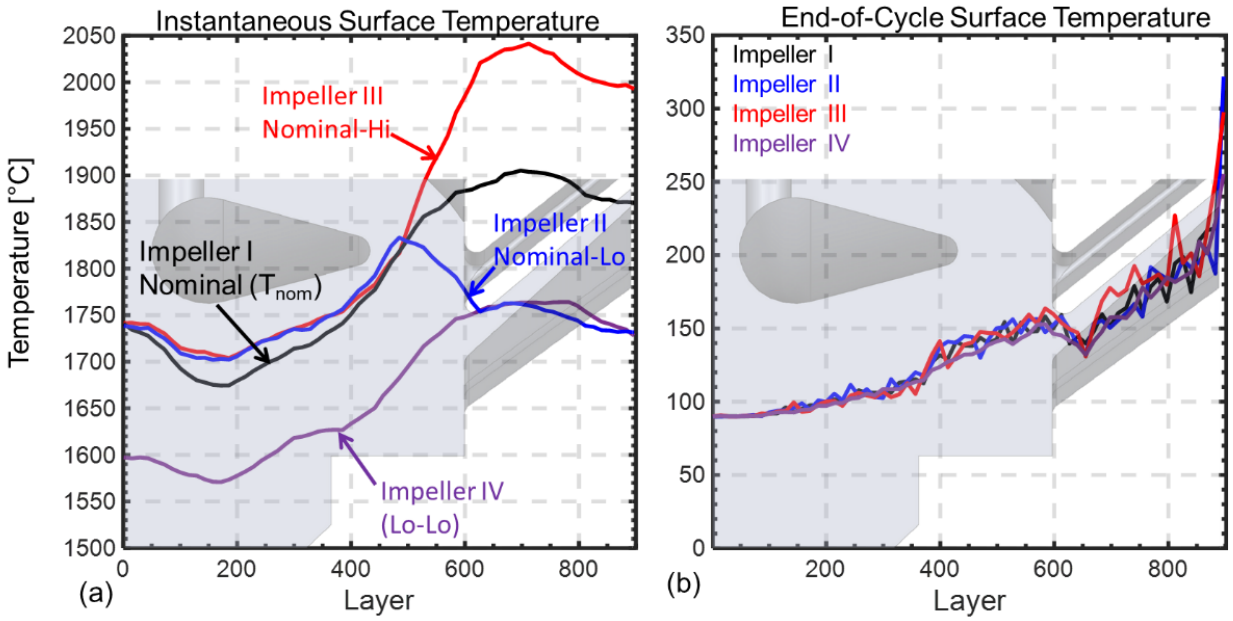

Figure 29: (a) The thermal history for the four impellers on account of sampling the instantaneous surface temperature following 0.1 seconds after the laser strike. The thermal trends diverge significantly corresponding to the change in the laser power in the fin region. (b) When the thermal simulation is sampled at the end-of-cycle, the difference between the four impellers is not evident.

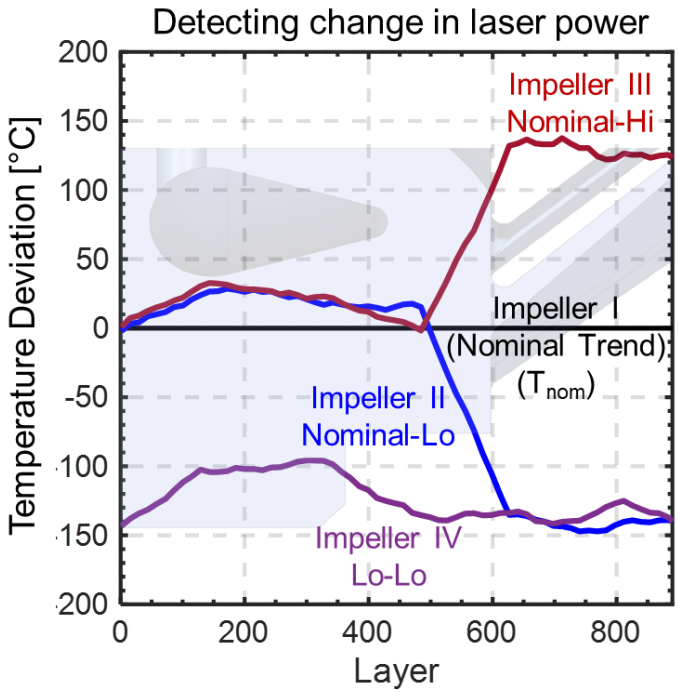

Figure 30: The temperature deviations from the nominal Impeller I are used to detect process drifts. As the laser power in the processing of the fin region changes for Impeller II and III, the layer temperature deviates significantly from that of the nominal flaw-free Impeller I. Likewise, the temperature trends for Impeller IV, which is produced at low power (125 W) is significantly different than the nominal impeller I.

3.3.2 Case II – Detecting Planted Flaws (cyber intrusions)

Next, in Figure 31(a) and (b), the digital twin approach is used for detecting the implanted flaws (voids) in Impeller II and Impeller III, respectively. Referring to Figure 31(a), a significant difference in the thermal trends between Impeller I and Impeller II is noted. Further, within the thermal trends for Impeller II, there is a large difference in the region where flaws are embedded, in contrast to thermal trends from flaw-free regions of Impeller II.

The deviation from the thermal trends of the flaw-free region is the largest at the location corresponding to biggest embedded flaw of Φ 0.5 mm. A similar difference between is noted in the thermal trends of Impeller III in Figure 31(b) for regions with and without embedded flaws. These large deviations in the thermal trends makes it is possible to readily identify when malicious intrusions have occurred, as well as pinpoint which regions have been targeted. Shown, in Figure 32 are deviations ($T_{new} - T_{nom}$) in the thermal history for Impellers III and IV relative to Impeller I sampled in the region with planted (embedded) flaws. The temperature deviations are significant in the region with embedded flaws, as well as in the region where the fins are built with changed processing parts.

From Figure 31 and Figure 32, a temperature deviation exceeding 40 °C to 50 °C from the nominal thermal history were correlated to flaw formation. However, referring to Figure 32, there is limitation in the smallest size of the flaw that can be detected in the current embodiment of the digital twin approach. Imposing a deviation threshold of 40 °C, flaws larger than a diameter of 100 μm were readily detected. This flaw detection limit is influenced by the layer resolution of the graph theory model, viz., 250 μm (Figure 18(b)). Improving the model resolution, would therefore improve the detection ability, albeit at the cost of computation time.

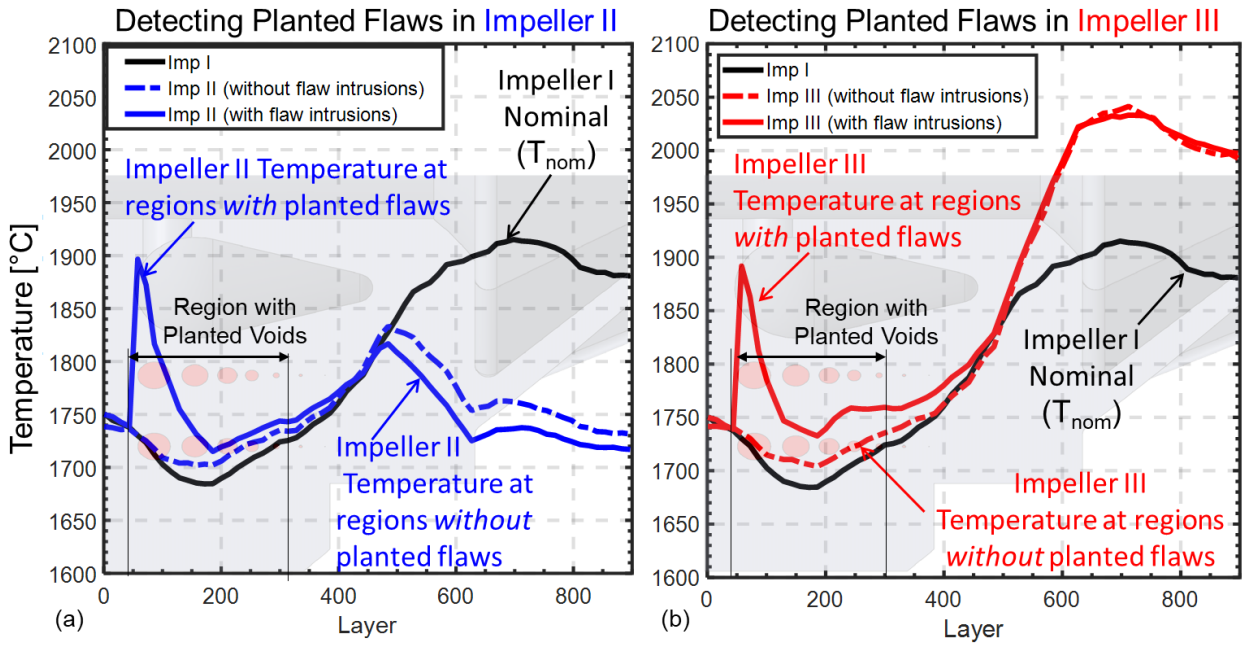

Figure 31: The temperature response for Impeller II and III sampled at sections where flaws were planted. (a) There is not only a distinct difference in the thermal history of Impeller I and Impeller II, but also in the thermal history of sections with and without implanted flaws. There is a noticeable increase in the temperature in the region where flaws are embedded.

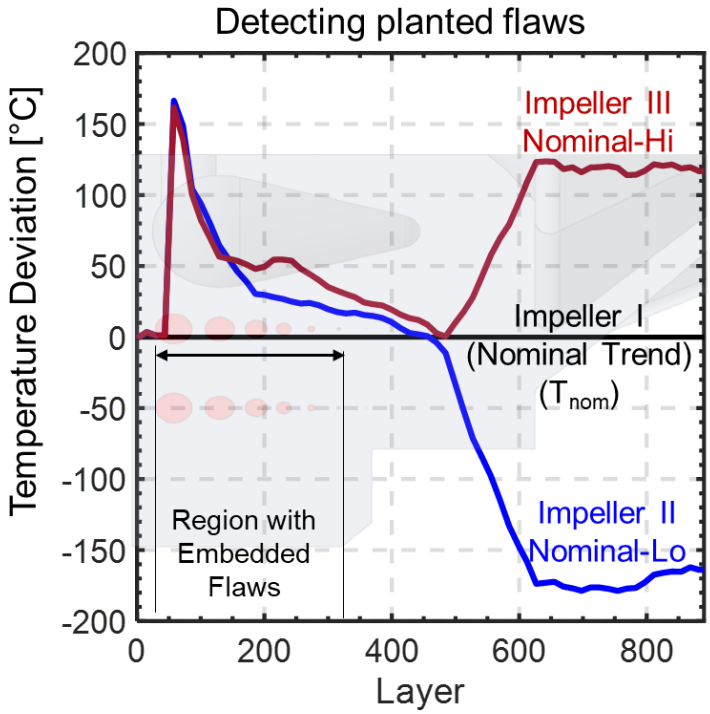

Figure 32: A large deviation from the nominal temperature trends is observed in the region where there are embedded flaws.

3.3.3 Case III – Detecting lens delamination (machine faults)

The implementation of the digital twin for detecting lens delamination is shown in Figure 33. Plotted in Figure 33(a) are the thermal history trends for Impeller III with the TEP data sampled in the region with delamination. Also overlaid are thermal trends for Impeller III sampled for the flaw-free region, as well as the thermal history for the nominal, flaw-free Impeller I.

The deviation in thermal history of Impeller III from Impeller I are reported in Figure 33(b). The temperature trend of Impeller III in the regions of delamination not only deviate significantly from those of Impeller I, but also from the thermal trends for delamination-free regions of Impeller III These results affirm that the digital twin approach captures the difference in temperature trends that are symptomatic of flaw formation between different impellers, but also within the same impeller on account of machine faults.

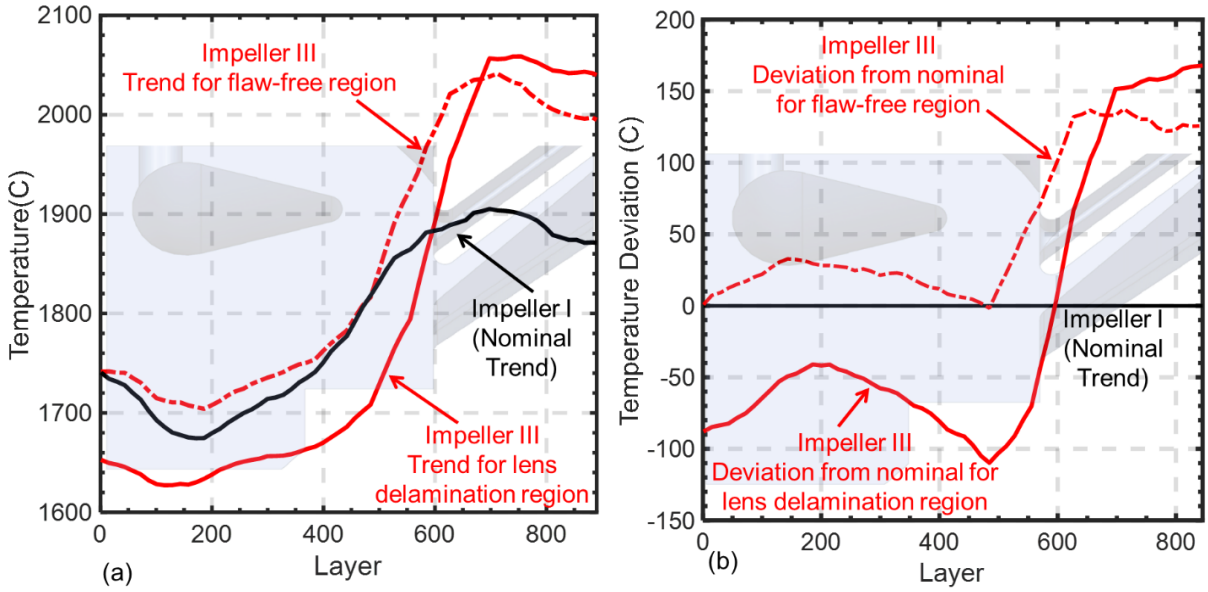

Figure 33:(a) The thermal history trends for Impeller III sampled from the lens delamination region, compared to thermal history trends for the flaw-free region. Shown also is the trend for the nominal, flaw-free Impeller I. (b) There is a large deviation from the nominal trends (Impeller I) where lens delamination is observed in Impeller III. The deviation in the thermal trends is also when regions affected by delamination are compared to delamination-free regions for Impeller III.

4 Conclusions

This work demonstrates a digital twin strategy for in-situ flaw detection in laser powder bed fusion (LPBF) process. The digital twin herein refers to the combining of in-process meltpool temperature measured using an in-situ sensor array with fast part-level thermal models predicted using graph theory. Results demonstrate that the digital twin approach facilitates precise and interpretable detection of flaw formation as opposed to the use of sensor data alone. A key outcome is that the digital twin approach overcomes the need for transferring sensor signatures to a separate data analysis algorithm, thus precluding the inherent latency in data-driven flaw detection.

Specific outcomes and conclusions are as follows:

(1) To test the *digital twin* approach, four stainless steel (316L) impeller-shaped parts were built simultaneously on a EOS M290 LPBF system. These impellers measured Φ60 mm × 16.9 mm in height, consisted of 845 layers and required approximately 16.5 hours to complete. During the build, the process was monitored continuously using an array of three coaxial photodetectors integrated into the laser path. Signals obtained from the sensor array were processed to create two types of measurements, namely TEP and TED. The TEP signature is correlated to the meltpool temperature, while TED captures the broadband chamber radiation.

(2) The first of these four impellers, Impeller I, was produced under optimal processing parameters – nominally flaw-free processing conditions (laser power of 195 W). Two other impellers (Impeller II and III) were processed under differing laser power settings that were changed during the build to mimic process faults. For Impeller II, the laser power was changed from 195 W to 125 W; for Impeller III the laser power was changed from 195 W to 265 W. A fourth impeller, Impeller IV, was processed entirely under the reduced laser power of 125 W throughout. Further, voids were embedded into Impellers II, III, and IV to imitate flaw

formation caused due to malicious intrusions in the process. A third type of flaw, resulting from a type of machine anomaly called lens delamination was introduced in Impeller III, which led to reduced energy in the melting of specific regions.

(3) The impellers were characterized with non-destructive X-ray computed tomography (XCT), optical micrography, scanning electron microscopy, and electron backscatter diffraction. The XCT analysis revealed that the flaw volume ratio in the sample produced under nominal processing conditions (Impeller I) was under 0.01 percent, while for the rest of the impellers the flaw volume ratio was in the range of 0.08 percent to 0.11 percent. The optical and scanning electron microscopy revealed the presence of lack-of-fusion flaw formation in the functionally critical fin region of Impellers II, III, and IV. Differences in the microstructure (grain size and texture), and orientation were also evident for the four impellers using electron backscatter diffraction. Hence, a change in the processing conditions is liable to impact the functional integrity of a LPBF produced part.

(4) The thermal model used in this work was based on the novel concept of heat diffusion on graphs – graph theory, which was demonstrated to be several-fold faster than FE analysis [22, 44, 46-48]. The graph theory approach is used to predict the temperature distribution at the part level (thermal history). The graph theory simulation converged within 7 minutes compared to the 16.5 hour build time.

(5) The TEP and TED sensor signatures from the sensor data were incorporated into the graph theory model. In this manner, the part-level or macro-scale thermal history of the part predicted from graph theory is updated with micro-scale meltpool-level phenomena measured using in-process sensors. The proposed digital twin approach captured all three types of flaw formation aspects in an unambiguous manner. In its current embodiment, the approach is shown capable

of detecting planted flaws of diameter 100 μm and above. This limitation is readily remedied by increasing the resolution of the thermal simulation.

In our future work, we will endeavor to extend the digital twin for detecting various other types of flaws, such as distortion and recoater crash, as well as test the approach with different processing parameters, scanning strategies and part shapes.

Acknowledgements

Harold (Scott) Halliday thanks the NSF for funding the work carried out at Navajo Technical University through HRD 1840138 (NTU Center for Advanced Manufacturing). Prahalada Rao thanks the National Science Foundation (NSF) for funding his work under awards PFI-TT 2044710, OIA-1929172, CMMI-1719388, CMMI-1920245, CMMI-1739696, and CMMI-1752069. Predicting the thermal history of LPBF parts was the major aspect of PFI-TT 2044710 (Program Officer: Jose Colom-Ustariz) and CMMI-1752069 (Program Officer: Kevin Chou). Supplemental funding for CMMI-1752069 obtained through the NSF INTERN program (Program Officer: Prakash Balan) and CMMI Data Science Activities (Program Officer: Martha Dodson) is greatly appreciated. The NSF INTERN supplement funded a large part of Reza Yavari's research. The authors thank Autodesk for providing an academic license of their Netfabb software.

Data Availability Statement

The raw/processed data required to reproduce these findings cannot be shared at this time as the data also forms part of an ongoing study.

References Cited

[1] W. J. Sames, F. List, S. Pannala, R. R. Dehoff, and S. S. Babu, "The metallurgy and processing science of metal additive manufacturing," *International Materials Reviews,* vol. 61, pp. 315-360, 2016.

[2] B. H. Jared, M. A. Aguilo, L. L. Beghini, B. L. Boyce, B. W. Clark, A. Cook, B. J. Kaehr, and J. Robbins, "Additive manufacturing: Toward holistic design," *Scripta Materialia,* vol. 135, pp. 141-147, 2017/07/01/ 2017.

[3] M. Grasso and B. M. Colosimo, "Process defects andin situ monitoring methods in metal powder bed fusion: a review," *Measurement Science and Technology,* vol. 28, p. 044005, 2017/02/15 2017.

[4] M. Seifi, M. Gorelik, J. Waller, N. Hrabe, N. Shamsaei, S. Daniewicz, and J. J. Lewandowski, "Progress Towards Metal Additive Manufacturing Standardization to Support Qualification and Certification," *JOM,* vol. 69, pp. 439-455, 2017.

[5] Z. Snow, A. R. Nassar, and E. W. Reutzel, "Invited Review Article: Review of the formation and impact of flaws in powder bed fusion additive manufacturing," *Additive Manufacturing,* vol. 36, p. 101457, 2020/12/01/ 2020.
[6] A. du Plessis, I. Yadroitsava, and I. Yadroitsev, "Effects of defects on mechanical properties in metal additive manufacturing: A review focusing on X-ray tomography insights," *Materials & Design,* vol. 187, p. 108385, 2020/02/01/ 2020.
[7] H. Taheri, M. R. B. M. Shoaib, L. W. Koester, T. A. Bigelow, P. C. Collins, and L. J. Bond, "Powder-based additive manufacturing-a review of types of defects, generation mechanisms, detection, property evaluation and metrology," *International Journal of Additive and Subtractive Materials Manufacturing,* vol. 1, pp. 172-209, 2017.
[8] A. T. Polonsky and T. M. Pollock, "Closing the science gap in 3D metal printing," *Science,* vol. 368, p. 583, 2020.
[9] M. Mani, B. M. Lane, M. A. Donmez, S. C. Feng, and S. P. Moylan, "A review on measurement science needs for real-time control of additive manufacturing metal powder bed fusion processes," *International Journal of Production Research,* vol. 55, pp. 1400-1418, 2017/03/04 2017.
[10] H. Yang, P. Rao, T. Simpson, Y. Lu, P. Witherell, A. R. Nassar, E. Reutzel, and S. Kumara, "Six-Sigma Quality Management of Additive Manufacturing," *Proceedings of the IEEE,* vol. 109, pp. 347-376, 2021.
[11] T. G. Spears and S. A. Gold, "In-process sensing in selective laser melting (SLM) additive manufacturing," *Integrating Materials and Manufacturing Innovation,* vol. 5, pp. 16-40, 2016/12/01 2016.
[12] Y. Huang, M. C. Leu, J. Mazumder, and A. Donmez, "Additive Manufacturing: Current State, Future Potential, Gaps and Needs, and Recommendations," *Journal of Manufacturing Science and Engineering,* vol. 137, 2015.
[13] A. Gaikwad, B. Giera, G. M. Guss, J.-B. Forien, M. J. Matthews, and P. Rao, "Heterogeneous sensing and scientific machine learning for quality assurance in laser powder bed fusion – A single-track study," *Additive Manufacturing,* vol. 36, p. 101659, 2020/12/01/ 2020.
[14] S. A. Khairallah, A. T. Anderson, A. Rubenchik, and W. E. King, "Laser powder-bed fusion additive manufacturing: Physics of complex melt flow and formation mechanisms of pores, spatter, and denudation zones," *Acta Materialia,* vol. 108, pp. 36-45, 2016.
[15] M. Markl and C. Körner, "Multiscale Modeling of Powder Bed–Based Additive Manufacturing," *Annual Review of Materials Research,* vol. 46, pp. 93-123, 2016/07/01 2016.
[16] M. M. Francois, A. Sun, W. E. King, N. J. Henson, D. Tourret, C. A. Bronkhorst, N. N. Carlson, C. K. Newman, T. Haut, J. Bakosi, J. W. Gibbs, V. Livescu, S. A. Vander Wiel, A. J. Clarke, M. W. Schraad, T. Blacker, H. Lim, T. Rodgers, S. Owen, F. Abdeljawad, J. Madison, A. T. Anderson, J. L. Fattebert, R. M. Ferencz, N. E. Hodge, S. A. Khairallah, and O. Walton, "Modeling of additive manufacturing processes for metals: Challenges and opportunities," *Current Opinion in Solid State and Materials Science,* vol. 21, pp. 198-206, 2017/08/01/ 2017.
[17] W. King, A. Anderson, R. Ferencz, N. Hodge, C. Kamath, and S. Khairallah, "Overview of modelling and simulation of metal powder-bed fusion process at Lawrence Livermore National Laboratory," *Materials Science and Technology,* vol. 31, pp. 957-968, 2014.
[18] G. Repossini, V. Laguzza, M. Grasso, and B. M. Colosimo, "On the use of spatter signature for in-situ monitoring of Laser Powder Bed Fusion," *Additive Manufacturing,* vol. 16, pp. 35-48, 2017/08/01/ 2017.

[19] T. DebRoy, H. L. Wei, J. S. Zuback, T. Mukherjee, J. W. Elmer, J. O. Milewski, A. M. Beese, A. Wilson-Heid, A. De, and W. Zhang, "Additive manufacturing of metallic components – Process, structure and properties," *Progress in Materials Science,* vol. 92, pp. 112-224, 2018/03/01/ 2018.
[20] T. Mukherjee, H. L. Wei, A. De, and T. DebRoy, "Heat and fluid flow in additive manufacturing – Part II: Powder bed fusion of stainless steel, and titanium, nickel and aluminum base alloys," *Computational Materials Science,* vol. 150, pp. 369-380, 2018/07/01/ 2018.
[21] L. E. Criales, Y. M. Arısoy, B. Lane, S. Moylan, A. Donmez, and T. Özel, "Laser powder bed fusion of nickel alloy 625: Experimental investigations of effects of process parameters on melt pool size and shape with spatter analysis," *International Journal of Machine Tools and Manufacture,* vol. 121, pp. 22-36, 2017/10/01/ 2017.
[22] R. Yavari, Z. Smoqi, A. Riensche, B. Bevans, H. Kobir, H. Mendoza, H. Song, K. Cole, and P. Rao, "Part-scale Thermal Simulation of Laser Powder Bed Fusion Using Graph Theory: Effect of Thermal History on Porosity, Microstructure Evolution, and Recoater Crash " *Materials & Design,* vol. 204, pp. 109685-711, 2021.
[23] A. Bandyopadhyay and K. D. Traxel, "Invited review article: Metal-additive manufacturing—Modeling strategies for application-optimized designs," *Additive Manufacturing,* vol. 22, pp. 758-774, 2018/08/01/ 2018.
[24] Z. Luo and Y. Zhao, "A survey of finite element analysis of temperature and thermal stress fields in powder bed fusion Additive Manufacturing," *Additive Manufacturing,* vol. 21, pp. 318-332, 2018/05/01/ 2018.
[25] J. Shen, Z. Zeng, M. Nematollahi, N. Schell, E. Maawad, R. N. Vasin, K. Safaei, B. Poorganji, M. Elahinia, and J. P. Oliveira, "In-situ synchrotron X-ray diffraction analysis of the elastic behaviour of martensite and H-phase in a NiTiHf high temperature shape memory alloy fabricated by laser powder bed fusion," *Additive Manufacturing Letters,* vol. 1, p. 100003, 2021/12/01/ 2021.
[26] R. J. Williams, A. Piglione, T. Rønneberg, C. Jones, M.-S. Pham, C. M. Davies, and P. A. Hooper, "In situ thermography for laser powder bed fusion: Effects of layer temperature on porosity, microstructure and mechanical properties," *Additive Manufacturing,* vol. 30, p. 100880, 2019/12/01/ 2019.
[27] T. DebRoy, T. Mukherjee, H. L. Wei, J. W. Elmer, and J. O. Milewski, "Metallurgy, mechanistic models and machine learning in metal printing," *Nature Reviews Materials,* 2020/10/02 2020.
[28] B. Diehl and A. Nassar, "Reducing near-surface voids in metal (Ti-6Al-4V) powder bed fusion additive manufacturing: the effect of inter-hatch travel time," *Additive Manufacturing,* vol. 36, p. 101592, 2020/12/01/ 2020.
[29] M. Montazeri, R. Yavari, P. Rao, and P. Boulware, "In-Process Monitoring of Material Cross-Contamination Defects in Laser Powder Bed Fusion," *Journal of Manufacturing Science and Engineering,* vol. 140, 2018.
[30] N. Gupta, A. Tiwari, S. T. S. Bukkapatnam, and R. Karri, "Additive Manufacturing Cyber-Physical System: Supply Chain Cybersecurity and Risks," *IEEE Access,* vol. 8, pp. 47322-47333, 2020.
[31] J. P. Oliveira, A. D. LaLonde, and J. Ma, "Processing parameters in laser powder bed fusion metal additive manufacturing," *Materials & Design,* vol. 193, p. 108762, 2020/08/01/ 2020.

[32] L. D. Sturm, C. B. Williams, J. A. Camelio, J. White, and R. Parker, "Cyber-physical vulnerabilities in additive manufacturing systems: A case study attack on the .STL file with human subjects," *Journal of Manufacturing Systems,* vol. 44, pp. 154-164, 2017/07/01/ 2017.
[33] T. DebRoy, W. Zhang, J. Turner, and S. S. Babu, "Building digital twins of 3D printing machines," *Scripta Materialia,* vol. 135, pp. 119-124, 2017/07/01/ 2017.
[34] G. L. Knapp, T. Mukherjee, J. S. Zuback, H. L. Wei, T. A. Palmer, A. De, and T. DebRoy, "Building blocks for a digital twin of additive manufacturing," *Acta Materialia,* vol. 135, pp. 390-399, 2017/08/15/ 2017.
[35] T. Mukherjee and T. DebRoy, "A digital twin for rapid qualification of 3D printed metallic components," *Applied Materials Today,* vol. 14, pp. 59-65, 2019/03/01/ 2019.
[36] D. R. Gunasegaram, A. B. Murphy, A. Barnard, T. DebRoy, M. J. Matthews, L. Ladani, and D. Gu, "Towards developing multiscale-multiphysics models and their surrogates for digital twins of metal additive manufacturing," *Additive Manufacturing,* vol. 46, p. 102089, 2021/10/01/ 2021.
[37] S. S. Razvi, S. Feng, A. Narayanan, Y.-T. T. Lee, and P. Witherell, "A Review of Machine Learning Applications in Additive Manufacturing," in *ASME 2019 International Design Engineering Technical Conferences and Computers and Information in Engineering Conference*, 2019.
[38] C. Wang, X. P. Tan, S. B. Tor, and C. S. Lim, "Machine learning in additive manufacturing: State-of-the-art and perspectives," *Additive Manufacturing,* vol. 36, p. 101538, 2020/12/01/ 2020.
[39] J. A. Mitchell, T. A. Ivanoff, D. Dagel, J. D. Madison, and B. Jared, "Linking pyrometry to porosity in additively manufactured metals," *Additive Manufacturing,* vol. 31, p. 100946, 2020/01/01/ 2020.
[40] B. Lane, S. Moylan, P. Whitenton Eric, and L. Ma, "Thermographic measurements of the commercial laser powder bed fusion process at NIST," *Rapid Prototyping Journal,* vol. 22, pp. 778-787, 2016.
[41] G. Tapia and A. Elwany, "A Review on Process Monitoring and Control in Metal-Based Additive Manufacturing," *Journal of Manufacturing Science and Engineering,* vol. 136, 2014.
[42] F. Imani, A. Gaikwad, M. Montazeri, P. Rao, H. Yang, and E. Reutzel, "Process Mapping and In-Process Monitoring of Porosity in Laser Powder Bed Fusion Using Layerwise Optical Imaging," *Journal of Manufacturing Science and Engineering,* vol. 140, 2018.
[43] S. Liu, A. P. Stebner, B. B. Kappes, and X. Zhang, "Machine learning for knowledge transfer across multiple metals additive manufacturing printers," *Additive Manufacturing,* vol. 39, p. 101877, 2021/03/01/ 2021.
[44] R. Yavari, R. Williams, A. Riensche, P. A. Hooper, K. D. Cole, L. Jacquetmetton, H. Halliday, and P. Rao, "Thermal Modeling in Metal Additive Manufacturing using Graph Theory – Application to Laser Powder Bed Fusion of a Large Volume Impeller.," *Additive Manufacturing,* vol. 41, pp. 101956-74, 2021.
[45] R. Shi, S. Khairallah, T. W. Heo, M. Rolchigo, J. T. McKeown, and M. J. Matthews, "Integrated Simulation Framework for Additively Manufactured Ti-6Al-4V: Melt Pool Dynamics, Microstructure, Solid-State Phase Transformation, and Microelastic Response," *JOM,* vol. 71, pp. 3640-3655, 2019/10/01 2019.
[46] K. D. Cole, M. R. Yavari, and P. K. Rao, "Computational heat transfer with spectral graph theory: Quantitative verification," *International Journal of Thermal Sciences,* vol. 153, p. 106383, 2020/07/01/ 2020.

[47] M. R. Yavari, K. Cole, and P. Rao, "Thermal Modeling in Metal Additive Manufacturing using Graph Theory," *ASME Transactions, Journal of Manufacturing Science and Engineering,* vol. 141, pp. 071007-27, 2019.
[48] R. Yavari, R. J. Williams, K. D. Cole, P. A. Hooper, and P. Rao, "Thermal Modeling in Metal Additive Manufacturing Using Graph Theory: Experimental Validation With Laser Powder Bed Fusion Using In Situ Infrared Thermography Data," *Journal of Manufacturing Science and Engineering,* vol. 142, 2020.
[49] A. Gaikwad, R. Yavari, M. Montazeri, K. Cole, L. Bian, and P. Rao, "Toward the digital twin of additive manufacturing: Integrating thermal simulations, sensing, and analytics to detect process faults," *IISE Transactions,* vol. 52, pp. 1204-1217, 2020/11/01 2020.
[50] O. Diegel, A. Nordin, and D. Motte, *A Practical Guide to Design for Additive Manufacturing*. Singapore: Springer, 2019.
[51] G. Bi, B. Schürmann, A. Gasser, K. Wissenbach, and R. Poprawe, "Development and qualification of a novel laser-cladding head with integrated sensors," *International Journal of Machine Tools and Manufacture,* vol. 47, pp. 555-561, 2007/03/01/ 2007.
[52] U. Thombansen, A. Gatej, and M. Pereira, "Process observation in fiber laser–based selective laser melting," *Optical Engineering,* vol. 54, p. 011008, 2014.
[53] V. R. Dave, D. D. Clark, M. Roybal, M. J. Cola, M. S. Piltch, R. B. Madigan, and A. Castro, "Multi-sensor quality inference and control for additive manufacturing processes," US 10,786,948 B2, 2020.
[54] V. R. Dave, M. J. Cola, R. B. Madigan, A. Castro, G. Wikle, L. Jacquemetton, and P. Campbell, "Systems and methods for additive manufacturing operations," US 10,717,264 B2, Jul. 21, 2020, 2019.
[55] C. B. Stutzman, W. F. Mitchell, and A. R. Nassar, "Optical emission sensing for laser-based additive manufacturing—What are we actually measuring?," *Journal of Laser Applications,* vol. 33, p. 012010, 2021.
[56] M. Montazeri, A. R. Nassar, A. J. Dunbar, and P. Rao, "In-process monitoring of porosity in additive manufacturing using optical emission spectroscopy," *IISE Transactions,* vol. 52, pp. 500-515, 2020/05/03 2020.
[57] M. Montazeri, A. R. Nassar, C. B. Stutzman, and P. Rao, "Heterogeneous sensor-based condition monitoring in directed energy deposition," *Additive Manufacturing,* vol. 30, p. 100916, 2019/12/01/ 2019.
[58] P. A. Hooper, "Melt pool temperature and cooling rates in laser powder bed fusion," *Additive Manufacturing,* vol. 22, pp. 548-559, 2018/08/01/ 2018.
[59] M. Gouge and P. Michaleris, *Thermo-Mechanical Modeling of Additive Manufacturing*. Cambridge, MA: Elsevier, 2018.
[60] P. Foteinopoulos, A. Papacharalampopoulos, and P. Stavropoulos, "On thermal modeling of Additive Manufacturing processes," *CIRP Journal of Manufacturing Science and Technology,* vol. 20, pp. 66-83, 2018/01/01/ 2018.
[61] B. Schoinochoritis, D. Chantzis, and K. Salonitis, "Simulation of metallic powder bed additive manufacturing processes with the finite element method: A critical review," *Proceedings of the Institution of Mechanical Engineers, Part B: Journal of Engineering Manufacture,* vol. 231, pp. 96-117, 2017/01/01 2015.
[62] E. R. Denlinger, M. Gouge, and P. Michaleris, *Thermo-Mechanical Modeling of Additive Manufacturing*: Butterworth-Heinemann, 2018.

[63] R. Ganeriwala and T. I. Zohdi, "Multiphysics modeling and simulation of selective laser sintering manufacturing processes," *Procedia CIRP,* vol. 14, pp. 299-304, 2014.
[64] R. Ganeriwala and T. I. Zohdi, "A coupled discrete element-finite difference model of selective laser sintering," *Granular Matter,* vol. 18, p. 21, 2016.
[65] H. Peng, M. Ghasri-Khouzani, S. Gong, R. Attardo, P. Ostiguy, B. A. Gatrell, J. Budzinski, C. Tomonto, J. Neidig, M. R. Shankar, R. Billo, D. B. Go, and D. Hoelzle, "Fast prediction of thermal distortion in metal powder bed fusion additive manufacturing: Part 1, a thermal circuit network model," *Additive Manufacturing,* vol. 22, pp. 852-868, 2018/08/01/ 2018.
[66] Y. A. Çengel, & Ghajar, A. J, *Heat and Mass Transfer: Fundamentals & applications.*: New York: McGraw Hill, 2011.
[67] P. Bidare, I. Bitharas, R. M. Ward, M. M. Attallah, and A. J. Moore, "Fluid and particle dynamics in laser powder bed fusion," *Acta Materialia,* vol. 142, pp. 107-120, 2018/01/01/ 2018.
[68] T. Kurzynowski, K. Gruber, W. Stopyra, B. Kuźnicka, and E. Chlebus, "Correlation between process parameters, microstructure and properties of 316 L stainless steel processed by selective laser melting," *Materials Science and Engineering: A,* vol. 718, pp. 64-73, 2018.
[69] O. Andreau, I. Koutiri, P. Peyre, J.-D. Penot, N. Saintier, E. Pessard, T. De Terris, C. Dupuy, and T. Baudin, "Texture control of 316L parts by modulation of the melt pool morphology in selective laser melting," *Journal of Materials Processing Technology,* vol. 264, pp. 21-31, 2019.
[70] J. P. Oliveira, T. M. Curado, Z. Zeng, J. G. Lopes, E. Rossinyol, J. M. Park, N. Schell, F. M. Braz Fernandes, and H. S. Kim, "Gas tungsten arc welding of as-rolled CrMnFeCoNi high entropy alloy," *Materials & Design,* vol. 189, p. 108505, 2020/04/01/ 2020.